CDF/ANAL/ELECTROWEAK/CDFR/1216

Version 1.0

The Forward–Backward Asymmetry and $\sin^2\theta_W$

P. Hurst, M. Franklin, E. Kearns, J. Ng

May 31, 1990

Abstract

This note describes a measurement of $\sin^2\theta_W$ based on the charge asymmetry in the reaction $p\bar{p} \to Z^0 \to e^+e^-$. Using 250 Z^0 candidates we find $\sin^2\theta_W = 0.231 \pm 0.016$ (stat) $\pm\, 0.002$(sys), after QED corrections. Systematic errors and radiative corrections to the asymmetry are found to be small. Renormalization effects in the interpretation of $\sin^2\theta_W$ depend strongly on the top mass and can be large. This result is consistent with world average value of $\sin^2\theta_W$, both with and without radiative corrections.

1 Introduction

In the Standard Model of electroweak interactions [1], the neutral current is described as a mixture of the weak isospin and electromagnetic currents, with "mixing angle" θ_W, as shown below:

$$J_\mu^{NC} = J_\mu^{I_3} - \sin^2\theta_W J_\mu^{EM}. \tag{1}$$

The weak isospin component of the neutral current leads to a parity violating V − A form for the neutral current interaction, which is then slightly modified by the electromagnetic current. The vertex factor for the neutral interaction is given by

$$\frac{-ig}{\cos\theta_W}\gamma^\mu\frac{1}{2}(g_V^f - g_A^f\gamma^5) \tag{2}$$

where the vector and axial vector fermion couplings g_V^f and g_A^f are given by

$$g_V^f = T_f^3 - 2Q_f\sin^2\theta_W \qquad g_A^f = T_f^3 \tag{3}$$

taking T_f^3 and Q_f to be the third component of weak isospin and the charge of the fermion, respectively. Due to the V − A form of the interaction, the Z^0 couples more strongly to left–handed fermions and right–handed antifermions. Using helicity and angular momentum conservation arguments similar to those used for charged current processes, one finds that in $f\bar{f} \to Z^0 \to f'\bar{f}'$ interactions the outgoing fermion (antifermion) is preferentially emitted in the direction of the incoming fermion (antifermion). This implies that there will be a charge asymmetry in the decay angular distribution of the Z^0, and furthermore that the magnitude of this asymmetry depends on the values of the vector and axial vector couplings of the Z^0. In the Standard Model, the vector and axial vector couplings themselves depend only on $\sin^2\theta_W$ and the (known) values of charge and isospin, and so one can infer a value for $\sin^2\theta_W$ from a measurement of the charge asymmetry in Z^0 decays. We propose, then, to determine $\sin^2\theta_W$ from a measurement of the dielectron angular distribution in $p\bar{p} \to Z^0 \to e^+e^-$ events at CDF.

At lowest order, both photon exchange and Z^0 exchange contribute to electron pair production in hadronic collisions; the Feynman diagrams for these processes are shown in Figure 1. A calculation based on these diagrams gives the cross section [2, 3]

$$\begin{aligned}\frac{d\sigma}{d\cos\hat{\theta}} = N_C^f \; & \int_0^1 dx_a \int_0^1 dx_b \sum_q q(x_a,\hat{s})\bar{q}(x_b,\hat{s}) \Bigg\{ \frac{\pi\alpha^2 Q_q^2}{2\hat{s}}(1+\cos^2\hat{\theta}) \\ & - \frac{\alpha Q_q G_F M_Z^2(\hat{s}-M_Z^2)}{2\sqrt{2}[(\hat{s}-M_Z^2)^2+M_Z^2\Gamma_Z^2]}[g_V^e g_V^q(1+\cos^2\hat{\theta}) + 2g_A^e g_A^q \cos\hat{\theta}] \\ & + \frac{G_F^2 M_Z^4 \hat{s}}{16\pi[(\hat{s}-M_Z^2)^2+M_Z^2\Gamma_Z^2]} \\ & \times [((g_V^e)^2+(g_A^e)^2)((g_V^q)^2+(g_A^q)^2)(1+\cos^2\hat{\theta}) + 8g_V^e g_A^e g_V^q g_A^q \cos\hat{\theta}] \Bigg\}\end{aligned} \tag{4}$$

where $\hat{\theta}$ is defined to be the angle between the outgoing electron and incoming quark (or outgoing positron and incoming antiquark) in the rest frame of the electron pair. Note that N_C^f is a color factor, $q(x_a,\hat{s})$ and $\bar{q}(x_b,\hat{s})$ are the quark distribution functions in the proton and antiproton, and the sum is over quark species. The first and third terms in the cross section are due to photon exchange and Z^0 exchange, respectively, while the second term arises from the quantum mechanical interference of these two subprocesses. Each term has a symmetric component proportional to $(1+\cos^2\hat{\theta})$, and both the Z^0 and interference terms have antisymmetric components proportional to $\cos\hat{\theta}$. While the interference term is important in the charge asymmetries seen away from the Z^0, its contribution to the cross section near the Z peak is small (of order 1% of the total cross section). We wish to emphasize that the asymmetry seen in $p\bar{p} \to e^+e^-$ events at the Z^0 resonance is a feature of the Z^0 couplings to fermions, and is not merely an interference effect.

A useful quantity is the forward–backward asymmetry at the Z^0 resonance, A_{FB}, defined by

$$A_{\mathrm{FB}} = \frac{\int_0^1 \frac{d\sigma}{d\cos\hat{\theta}}\, d(\cos\hat{\theta}) - \int_{-1}^0 \frac{d\sigma}{d\cos\hat{\theta}}\, d(\cos\hat{\theta})}{\int_{-1}^1 \frac{d\sigma}{d\cos\hat{\theta}}\, d(\cos\hat{\theta})}. \tag{5}$$

The asymmetry in $p\bar{p} \to e^+e^-$ is a function of both the quark couplings and the lepton couplings to the Z^0. Unlike the purely leptonic asymmetry measurements soon to be made at LEP, a measurement of $A_{\rm FB}$ at CDF is an indirect measurement of the Z^0 couplings to light quarks. Furthermore, we note that the vector coupling to leptons is very near zero for $\sin^2\theta_W$ values near 0.25, and so the expected asymmetry for interactions involving leptons is small. The purely leptonic asymmetries at LEP involve two factors of this small coupling constant, and so are expected to be significantly smaller than the quark–lepton asymmetries observed at CDF. At CDF, however, collisions involve protons, not bare quarks. Since the u–type and d–type quark couplings to Z^0's are different, the observed asymmetry is sensitive to the flavor content of the protons. The expected asymmetries are therefore a function of the structure functions of the proton. Figure 2. shows the asymmetry as a function of $\sin^2\theta_W$ for u–type and d–type quarks. In the region near $\sin^2\theta_W = 0.230$, the u and d quark asymmetries are nearly equal, and so we expect that the observed asymmetry will not depend strongly on the u to d quark ratio.

Finally, we note that when higher order diagrams are included, both the observed asymmetry and the precise definition of $\sin^2\theta_W$ will change. Some of the higher order diagrams are asymmetric in their own right, and their contributions to $d\sigma/d\cos\hat{\theta}$ must be calculated. Furthermore, when higher order effects are included, values for $\sin^2\theta_W$ determined from different physical processes get different corrections and are no longer directly comparable [4]. In particular, the value of $\sin^2\theta_W$ determined from the charge asymmetry is not directly comparable to the value determined by $1 - M_W^2/M_Z^2$ until higher order corrections are made and a particular form for $\sin^2\theta_W$ is adopted.

2 Measuring $\cos\hat{\theta}$

There are a number of factors which are of importance in measuring $\cos\hat{\theta}$. First, recall that $\hat{\theta}$ is defined to be the angle between the outgoing electron and incoming quark (or outgoing positron and incoming antiquark) in the Z^0 rest frame. Since this definition requires us to differentiate between the electron and the positron, we must be able to measure the charge of at least one of the electrons in the event. This requires that at least one of the electrons is produced in the central region and leaves a well reconstructed track in the drift chamber.

Next, $\hat{\theta}$ is properly defined by the quark and antiquark directions. In practice, we know the directions of the protons and antiprotons only; we assume that the initial quark is moving in the proton direction and the initial antiquark is moving in the antiproton direction. While this is always true for interactions involving valence quarks, it is wrong half the time for interactions in which both quarks come from the Fermi sea. Since the sign of $\cos\hat{\theta}$ is mismeasured for half of the sea–sea interactions, the sea–sea interactions give a symmetric "background" contribution to the angular distribution. Any determination of $\sin^2\theta_W$ from the asymmetry, then, will depend on the sea–sea contribution, and therefore on the proton structure functions. The total observed asymmetry for EHLQ 1 structure functions is shown in Figure 2. The effect of the symmetric sea–sea contribution is to reduce the observed asymmetry.

Finally, due to QCD effects such as initial state gluon bremsstrahlung, the Z^0's are produced with varying amounts of transverse momentum, P_T. When a Z^0 is produced with non–zero P_T, the proton and antiproton directions are not collinear in the rest frame of the dileptons, and so the quark directions are not completely determined; the quarks can only be said to be travelling in approximately the direction of the proton or antiproton, and the approximation gets worse as P_T increases. Since the initial quark directions are ill–defined, $\cos\hat{\theta}$ can no longer be precisely measured. One must therefore define a new $\hat{z}$ axis in the dilepton rest frame to take the place of the quark direction when making angular measurements. Several definitions have been proposed [5], among them the helicity frame in which the $\hat{z}$ axis is taken along the recoil direction of the Z^0, and the Gottfried–Jackson frame in which the $\hat{z}$ axis is taken along the proton direction. We choose to use the method of Collins and Soper [6], in which the $\hat{z}$ axis is taken to be the bisectrix of the proton and minus the antiproton directions. In effect, the Collins–Soper definition divides the P_T contribution equally between the quark and antiquark, and possesses the feature that $\hat{z}$ reduces to the (known) quark direction in the limit $P_T \rightarrow 0$. All of these definitions are approximations which begin to break down at high values of P_T. We thus expect that the $\cos\hat{\theta}$ distribution will be smeared somewhat by the high P_T events. The size of this smearing and its effect on our result is discussed in Section 8.

3 Data Sample

The data sample is taken from the electron mini–DST's made by Production (ELM00 and ELM01). We make the energy corrections contained in the ELENCR [7] routine and recalculate strip quantities with STRFIX [8]. We make fiducial cuts using the latest version of FIDELE [9], and track related quantities are calculated using beam constrained tracks. We require the events to pass the Electron_12 trigger. The normal range of bad runs was excluded. For the asymmetry analysis we require each event to have one high quality CEM electron with a second good electron anywhere in the detector. The electron quality cuts shown in Table 1. We find 303 events which pass these dielectron cuts. A plot of dielectron invariant mass for these events is shown in Figure 3. The Z^0 peak is prominent, and backgrounds appear to be low. We take as our Z^0 sample the 250 events in the range 75 GeV $< M_{ee} <$ 105 GeV. A plot of $dn/d\cos\hat{\theta}$ for events satisfying the above electron quality and mass cuts is shown in Figure 4. There are more events with positive values of $\cos\hat{\theta}$ than negative values, as expected. Further, the $dn/d\cos\hat{\theta}$ distribution has the parabolic shape predicted by the cross section calculated previously. Note that the geometrical acceptance of the CDF detector falls off as $|\cos\hat{\theta}|$ approaches 1.0, and so we see a reduced number of events in the outermost bins of Figure 4.

We estimate the background for this data sample using the method developed by Kearns *et.al.* [10] for the $\sigma \cdot B$ analysis. Using the maximum isolation and the invariant mass distributions, and assuming a background flat in maximum isolation and mass, we estimate 6 ± 3 events due to non-dielectron backgrounds. We take the estimate of 0 $Z^0 \rightarrow \tau^+\tau^-$ events from the R paper.

Require one tight **CEM** electron:

E_t	$>$	15	GeV
E/p	$<$	1.5	
LSHR	$<$	.20	
χ^2_{strip}	$<$	15	
$\lvert\Delta x\rvert$	$<$	1.5	cm
$\lvert\Delta z\rvert$	$<$	3.0	cm
Iso(r=.4)	$<$	.10	

Require one additional electron:

If **CEM** electron:

E_t	$>$	15	GeV
E/p	$<$	1.5	
Iso(r=.4)	$<$	.10	

If **PEM** electron:

E_t	$>$	15	GeV
$\chi^2_{3\times3}$	$<$	20	
VTPC occupancy	$<$	0.5	cm
HAD/EM	$<$	.05	
Iso(r=.4)	$<$	.10	

If **FEM** electron:

E_t	$>$	15	GeV
E_{front}/E_{total}	$>$	.6	
HAD/EM	$<$	.05	
Iso(r=.4)	$<$	.10	

Table 1: Electron quality cuts

4 Acceptance issues

We use a Monte Carlo event generator and a simple detector simulation to determine the acceptance. The detector geometry and electron E_T cut are easily simulated. To simulate the electron quality cuts, we accept and reject events based on the measured efficiencies of the cuts rather than attempt a full simulation of the detector. The efficiencies used are

$$\begin{aligned} \epsilon_{\mathrm{CEM(tight)}} &= 0.850 \pm .025 \\ \epsilon_{\mathrm{CEM(loose)}} &= 0.891 \pm .023 \\ \epsilon_{\mathrm{PEM}} &= 0.931 \pm .021 \\ \epsilon_{\mathrm{FEM}} &= 0.957 \pm .025 \end{aligned}$$

The efficiencies for the PEM and FEM cuts are taken from the $\sigma \cdot B$ analysis of Reference been determined in the same fashion as those in Reference [10], but with the cuts listed in Table 1.

We calculate the $\cos\hat{\theta}$–dependent acceptance using generation–level 4–vectors from the ISAJET 6.22 Monte Carlo [11], using EHLQ1 structure functions. The steps in the acceptance calculation are as follows.

1. Generate $p\bar{p} \rightarrow e^+e^-$ events
2. Make histogram of $dn/d\cos\hat{\theta}$ using generated quantities for events with 75 GeV $<$ $M_{ee} <$ 105 GeV
3. Smear the event vertex with $\sigma_{\mathrm{vertex}} = 30.0$ cm
4. Extrapolate the electron 4-vectors to the detector.
5. Make fiducial cuts on the extrapolated position consistent with those made on the data.
6. Smear the electron energy by the calorimeter resolutions:

$$\begin{array}{llcccc} \mathrm{CEM} & \sigma_E/E & = & 0.135/\sqrt{E} & + & .007 \\ \mathrm{PEM} & \sigma_E/E & = & 0.28/\sqrt{E} & + & .002 \\ \mathrm{FEM} & \sigma_E/E & = & 0.28/\sqrt{E} & + & .002 \end{array}$$

7. Make the E_t cut on each electron (15 GeV).
8. Discard electrons in each detector based on the combined efficiencies for the electron quality cuts given above
9. Make histogram of $dn/d\cos\hat{\theta}$ using smeared quantities for events passing the above acceptance cuts and having 75 GeV $< M_{ee} <$ 105 GeV

10. The $\cos\hat{\theta}$ dependent acceptance is defined to be the bin–by–bin ratio of the histogram of step 9 and the histogram of step 2

Since the acceptance is symmetric with respect to $\cos\hat{\theta}$ at the generator level, we have combined histogram bins in a symmetric fashion in order to increase the statistical accuracy of our acceptance measurement. A plot of acceptance versus $\cos\hat{\theta}$ is shown in Figure 5. The acceptance is fairly flat in the region $|\cos\hat{\theta}| < 0.9$, but falls due to the CEM–PEM crack and fiducial cuts near $|\cos\hat{\theta}| = 0.25$ and due to the PEM–FEM crack and fiducial cuts near $|\cos\hat{\theta}| = 0.6$. The acceptance is significantly reduced for $|\cos\hat{\theta}| > 0.9$ for two reasons. First, the E_T's of the electrons in events with large values of $\cos\hat{\theta}$ tend to peak at low values, due to simple kinematics ($E_T \sim E\sin\hat{\theta}$), and so we lose a large number of these events due to the E_T cut. Second, the requirement that one of the electrons be located in the central region reduces the geometric acceptance for events with large values of $\cos\hat{\theta}$.

Finally, we note that if we simply exchange the identities of the electron and positron in any dielectron event, the event topology remains unchanged while $\cos\hat{\theta}$ changes sign. If the detector acceptance depends only on the event topology and not on the charges of the electrons, then the acceptance must be independent of the sign of $\cos\hat{\theta}$, and must therefore be symmetric with respect to $\cos\hat{\theta}$. Also, if we exchange the sign of η for each electron in the event (*i.e.* exchange east for west), then $\cos\hat{\theta}$ again changes sign. If the detector acceptance is east–west symmetric, then the acceptance is again independent of the sign of $\cos\hat{\theta}$, and must be symmetric with respect to $\cos\hat{\theta}$. In order for the acceptance to be asymmetric in $\cos\hat{\theta}$, the acceptance must be charge dependent, and the charge dependence must vary as a function of η. The effect of an asymmetric acceptance is discussed in Section 6.

5 Determining $\sin^2\theta_W$

We use three methods to determine $\sin^2\theta_W$ and A_{FB} from the $dn/d\cos\hat{\theta}$ distribution. Below we examine each of these methods, paying particular attention to the acceptance measured in the previous section. We will represent the lowest order cross section of Equation 4 by the simple form

$$\frac{d\hat{\sigma}}{d\cos\hat{\theta}} = A(1+\cos^2\hat{\theta}) + B\cos\hat{\theta} \tag{6}$$

where A and B are functions of $\sin^2\theta_W$ and include integrations over structure functions and kinematic variables. It is convenient for what follows to describe the detector acceptance by a function $\epsilon(\cos^2\hat{\theta})$ which is explicitly symmetric in $\cos\hat{\theta}$.

5.1 Negative log likelihood fit

Our method of choice for measuring $\sin^2\theta_W$ is a negative log likelihood fit to $dn/d\cos\hat{\theta}$. A disadvantage of the log likelihood fit is that there is no information about the quality of the fit. A major advantage, however is that the log likelihood minimization is independent of acceptance if the acceptance is symmetric in $\cos\hat{\theta}$.

To use the log likelihood method we begin with a normalized probability distribution function derived from the cross section of Equation 7:

$$P(\sin^2\theta_W, \cos\hat{\theta}) = \frac{3}{8}\left((1+\cos^2\hat{\theta}) + B/A\cos\hat{\theta}\right) \tag{7}$$

Note that all dependence on $\sin^2\theta_W$ is now contained in the B/A term. The acceptance is incorporated into the analysis by defining a new acceptance–corrected probability function which includes the acceptance function $\epsilon(\cos^2\hat{\theta})$:

$$P'(\sin^2\theta_W, \cos\hat{\theta}) = \frac{3}{8}N\epsilon(\cos^2\hat{\theta})\left((1+\cos^2\hat{\theta}) + B/A\cos\hat{\theta}\right) \tag{8}$$

where N is a normalization factor given by

$$\begin{aligned} N^{-1} &= \frac{3}{8}\int_{-1}^{1}\epsilon(\cos^2\hat{\theta})(1+\cos^2\hat{\theta})d\cos\hat{\theta} + \frac{3}{8}\int_{-1}^{1}\epsilon(\cos^2\hat{\theta})A/B\cos\hat{\theta}d\cos\hat{\theta} \\ &= \frac{3}{8}\int_{-1}^{1}\epsilon(\cos^2\hat{\theta})(1+\cos^2\hat{\theta})d\cos\hat{\theta} + \quad 0. \end{aligned} \tag{9}$$

Note that N is independent of $\sin^2\theta_W$. This acceptance–corrected function now describes the angular distribution measured with our detector and electron quality cuts. Finally, the likelihood, $\mathcal{L}$, and the negative log likelihood for a given data sample is defined by

$$\mathcal{L} = \prod_i N\epsilon_i(\cos^2\hat{\theta})P_i(\sin^2\theta_W, \cos\hat{\theta}) \tag{10}$$

$$-\ln\mathcal{L} = -\sum_i \ln(N\epsilon_i(\cos^2\hat{\theta})) - \sum_i \ln P_i(\sin^2\theta_W, \cos\hat{\theta}) \tag{11}$$

Once the data sample has been determined, the term $\sum \ln N\epsilon(\cos^2\hat{\theta})$ is a constant, independent of $\sin^2\theta_W$, and so does not affect the minimization of $-\ln\mathcal{L}$. For the negative log likelihood fit, then, the parameter estimation is independent of the acceptance.

We use the log likelihood method to fit the measured angular distribution to the form of the cross section given in Equation 4 and extract $\sin^2\theta_W$ directly. We find $\sin^2\theta_W = 0.232 \pm\ 0.016$ (stat). One can also fit the angular distribution to a simple parabolic form,

$$\frac{dn}{d\cos\hat{\theta}} = (1+\cos^2\hat{\theta}) + \beta\cos\hat{\theta} \tag{12}$$

and extract the forward–backward asymmetry from the fitted value of β using

$$A_{\mathrm{FB}} = \frac{3}{8}\beta. \tag{13}$$

Using this prescription, we find $A_{\mathrm{FB}} = 0.047 \pm 0.059$ (stat).

5.2 Binned χ^2 fit

The second method for measuring $\sin^2\theta_W$ is a binned χ^2 fit to an acceptance corrected histogram of $dn/d\cos\hat{\theta}$. The advantage of the χ^2 method is that the value of χ^2 gives some insight into the quality of the fit. This method, however, depends explicitly on the acceptance measured in Section 4. The measured distribution is corrected bin–by–bin by dividing the measured distribution by the acceptance factors measured in Section 4 and shown in Figure 5. We note that the corrections to the contents of the outermost bins are relatively large, and so small fluctuations in the contents of these bins can have a large effect on the distribution after the corrections are applied. We therefore exclude the two outermost bins from the χ^2 fit.

Fitting directly to the form of the cross section, we extract $\sin^2\theta_W = 0.234 \pm\ 0.017$ (stat) with a χ^2 of 8 for 28 degrees of freedom. Fitting to the simple parabolic form of Equation 13 we find $A_{\rm FB} = 0.041 \pm 0.064$ (stat), with a χ^2 of 8 for 28 degrees of freedom.

5.3 Event Counting

The third method is direct measurement of $A_{\rm FB}$ obtained simply by counting events. We adopt the definition

$$A_{FB}|_{direct} \equiv \frac{\mathrm{N}_{\cos\hat{\theta}>0} - \mathrm{N}_{\cos\hat{\theta}<0}}{\mathrm{N}_{\cos\hat{\theta}>0} + \mathrm{N}_{\cos\hat{\theta}<0}}. \tag{14}$$

This method of determining the asymmetry is also acceptance dependent, and so we calculate the asymmetry by first forming a bin–weighted histogram, and then summing the corrected bin contents. As with the binned χ^2, we get the best results if we exclude the bins nearest $|\cos\hat{\theta}| = 1.0$. We must therefore correct our result to conform to the definition of $A_{\rm FB}$ given in Equation 6. We extract a value for $\sin^2\theta_W$ by comparing the acceptance–corrected measured value of A_{FB} with the values predicted by given values of $\sin^2\theta_W$ and a particular choice of structure functions.

Using this direct method we find $A_{\rm FB} = 0.061 \pm 0.069$ (stat) after corrections. We use this result to determine $\sin^2\theta_W = 0.228 \pm 0.019$ (stat).

5.4 Summary of results

The results of the three methods are given in Table 2. The various values of $\sin^2\theta_W$ show good agreement, as do the statistical errors. The negative log likelihood is the preferred method for determining $\sin^2\theta_W$, because it is independent of the acceptance measurement, and it is the log likelihood value which we will quote below.

6 Systematics

There are several potential sources of systematic error on the asymmetry measurement, arising from both physics effects and detector effects. Below we discuss each in turn and estimate the size of these systematic effects.

Sumary of Fit Results CDF PRELIMINARY			
Method	$\sin^2\theta_W$	A_{FB}	χ^2/d.o.f.
Log likelihood	0.232 ± 0.016	0.047 ± 0.059	
Binned χ^2	0.234 ± 0.017	0.041 ± 0.064	8/28
Direct count	0.228 ± 0.019	0.061 ± 0.069	

Table 2: Results of the various parameter determinations

Systematic fit studies		
Method	$\sin^2\theta_W$	A_{FB}
Log likelihood	0.232 ± 0.018	0.050 ± 0.059
Binned χ^2	0.233 ± 0.018	0.051 ± 0.061
Direct count	0.232 ± 0.020	0.052 ± 0.068

Table 3: Mean and sigma of fits to multiple Monte Carlo data samples

6.1 Fitting systematics

We use a toy Monte Carlo to investigate possible biases in the fitting procedures. 500 data samples were generated according to a parabolic distribution. Each data sample contains 236 "events" which have been "accepted" based on the $\cos\hat{\theta}$ acceptance shown in Figure 5. We fit each sample, and make a distribution of the results. The mean of the distribution should agree with the input of the Monte Carlo, and the sigma of the distribution should agree with the statistical error on our real data sample. The results of these studies are given in Table 3. The means agree well with the Monte Carlo input parameters of $\sin^2\theta_W = 0.231$ and $A_{\mathrm{FB}} = 0.053$. The sigmas are comparable to those found for our data sample and shown in Table 2. We believe, then that our various methods of determining $\sin^2\theta_W$ and A_{FB} are not substantially biased.

6.2 Detector Effects

Since we use calorimeter cluster energies and centroids to measure the electron 4–vectors, the accuracy with which we can determine $\cos\hat{\theta}$ will be determined by the finite position and energy resolution of the detector. The position resolution of the calorimeter elements directly impacts on the measurement of $\cos\hat{\theta}$. In order to estimate the effect on $\sin^2\theta_W$ due to the finite position resolution of the calorimeters, we generated several (~ 100) 5pb^{-1} data samples with the ISAJET Monte Carlo, and imposed fiducial and E_T cuts. The generated electron 4–vectors were then smeared separately in x and y ($R\phi$ and z for the Central calorimeter) with a resolution of 2 cm at the face of each calorimeter. A value for $\sin^2\theta_W$

was then determined for each smeared data sample and then compared with the unsmeared value for the same sample. The values of $\sin^2\theta_W$ change by less than 0.0001 due to the finite position resolution of the detector.

Energy resolution and energy scale effects affect the $\cos\hat{\theta}$ measurement via the boost into the rest frame of the electron pair. In order to estimate the size of the effect due to the energy resolution of the calorimeter elements, the Monte Carlo generated data samples were smeared by the energy resolutions listed in Section 4. A value for $\sin^2\theta_W$ was then determined for each smeared data sample and then compared with the unsmeared value for the same sample. The values of $\sin^2\theta_W$ change by less than 0.0001 due to the finite energy resolution of the detector.

Energy scale changes were investigated by multiplying the Monte Carlo 4–vectors by detector–dependent scale factors. We note first that global energy scale changes do not affect the $\cos\hat{\theta}$ values, and so only energy scale differences were investigated. In the first test all the gas calorimeter energies were multiplied by 1.05. This 5% scale change causes the values of $\sin^2\theta_W$ to change by less than 0.0001. In the second test all the West calorimeter energies were multiplied by 1.05. Again, we find that the values of $\sin^2\theta_W$ change by less than 0.0001.

We conclude, then, that the detector resolutions have a negligible effect on the final result. The systematic error due to errors in the determination of the calorimeter energy scales is also negligible.

6.3 Background

If the background in the data sample is small and symmetric in $\cos\hat{\theta}$, the observed asymmetry is described by the simple relation

$$A_{\rm FB}|_{observed} = A_{\rm FB}|_{true} \cdot (1 - x), \tag{15}$$

where x is the fraction of background events in the sample. Using this relation and the estimate of 6 ± 3 non-dielectron background events from Section 3, we find that the observed forward–backward asymmetry is reduced by a relative 2.4%, and the measured value of $\sin^2\theta_W$ must be increased by 0.0006.

6.4 Charge Dependencies

It was argued in Section 4 that the acceptance is symmetric in $\cos\hat{\theta}$ if the detector is either charge–blind, or east–west symmetric. We assume that the calorimeters are charge independent, and can therefore introduce no charge asymmetry. There may, however, be charge and η dependent biases in the tracking quantities due to imperfections in the construction of the CTC, and so the size of these effects must be quantified.

The Electron_12 trigger has been measured to be 98.6% efficient [12]. From this, one can derive an upper limit on the shift in the asymmetry caused by charge dependencies in the trigger. If one assumes that the events which fail the trigger all have $\cos\hat{\theta}$ values with the same sign, then the asymmetry would be increased or decreased by 0.009. This implies a systematic error of 0.004 on $\sin^2\theta_W$. In fact, though, the situation is very much better than this. Any bias in the trigger or tracking will be due to physical imperfections in the central detector and therefore will depend on the physical position of a central electron. For any given central electron, the sign of $\cos\hat{\theta}$ can change depending on the second electron in the event. Any bias in $\cos\hat{\theta}$ due to the the central electron, then, is washed out by the second electron. A reliable estimate of the possible bias due to the trigger inefficiency therefore requres a Monte Carlo simulation. Using the ISAJET event generator, and assuming a central electron efficiency which depends linearly on the product of charge and detector η, one finds that the systematic error on $\sin^2\theta_W$ is less than 0.001. This value is an upper limit which is currently limited by the statistics of the Monte Carlo sample, and is expected to improve.

The track reconstruction efficiency has been shown by Alain Gauthier to be 99.86% efficient, based on a study of cosmic rays. Assuming all the events which fail have $\cos\hat{\theta}$ values with the same sign, one derives an upper limit of 0.003 on the change in the asymmetry, and and a systematic error on $\sin^2\theta_W$ of 0.001. Using the Monte Carlo and assuming the inefficiency is linear in the product of charge and detector η for central electrons, one finds the systematic error on $\sin^2\theta_W$ is limited by the Monte Carlo statistics at 0.001.

Craig Blocker has found similar results [13]. We conclude that the systematic error on A_{FB} and $\sin^2\theta_W$ due to biases in the trigger and tracking is very small.

6.5 Structure Functions

The exact functional form used in the fits depends on the relative contributions of u–type and d–type valence and sea quark production. While we use a reasonable choice for the proton structure functions in our calculation of $\sin^2\theta_W$, there are uncertainties in the structure function parametrizations, particularly at small x where the structure functions are not well–measured. In order to estimate the systematic error due to structure function uncertainties we have fit the data using several structure function parametrizations [14]. The results of the log likelihood fits are shown in Table 4, along with the u–type/d–type ratio and the ratio of sea–sea to valence interactions. We take the systematic error to be half the spread of the fitted values. The systematic error due to structure functions, then, is 0.00035

7 Comparisons with previous studies

A preliminary value for $\sin^2\theta_W$ from the forward–backward asymmetry has already been presented at several conferences and workshops [15]. The data for this preliminary study were taken from the Z_CAND.PRO_5_1 data file, and have been selected with the following cuts:

1. $E_T > 15$ GeV for both electrons
2. one central ($|\eta| < 1.0$) electron cluster with associated 3-D track and ratio of cluster energy to track momentum, $E/P < 2.0$.

Log–Likelihood Fit Results 1988–1989 Data CDF PRELIMINARY				
Parametrization	$\sin^2\theta_W$	Error	u/d Ratio	Sea/Valence
EHLQ 1	0.2321	0.0159	2.34	0.23
EHLQ 2	0.2321	0.0159	2.29	0.24
DO 1	0.2322	0.0163	1.58	0.30
DO 2	0.2316	0.0168	1.54	0.34
DFLM 1	0.2323	0.0158	2.09	0.24
DFLM 2	0.2322	0.0159	2.09	0.25
DFLM 3	0.2318	0.0159	2.16	0.25
MRSE	0.2322	0.0162	1.79	0.28
MRSB	0.2320	0.0162	1.96	0.27

Table 4: Fit results for various structure function parametrizations

3. lateral and longitudinal shower profiles consistent with an electron shower (*i.e.* Lshr < 0.5, $|\Delta z| < 5$cm in the CEM, $\chi^2_{3\times3} < 20$, $\chi^2_{Depth} < 20$ in the PEM, and $E_{front}/E_{total} > .6$ in the FEM)
4. Fiducial cuts made with FIDELE

The asymmetry measurement was made using only the 276 events in the mass range 76 GeV $< M_{ee} <$ 106 GeV, and yielded the value $\sin^2\theta_W = 0.216 \pm 0.015$. We must now determine if this result is consistent with the results obtained in Section 5. The comparison of these two results is complicated by the fact that the two data samples are not independent, but overlap to a large degree; of the 250 events in the Production sample used in the current analysis, 208 are also contained in the sample obtained from Z_CAND.PRO_5_1. It is not enough, then, to say that the two results agree within their statistical errors. We must account for the overlap in the samples when comparing the results.

We use our toy Monte Carlo to address the overlap issue. We generate pairs of data samples, one element having 250 events and the other having 276 events, with 208 overlapping events. We thus duplicate the conditions in our two data samples. We then fit each sample of the pair, and compare the results. The difference between the fitted values of $\sin^2\theta_W$ from the pairs of Monte Carlo samples should have a distribution peaked at zero, and the sigma of this distribution should be an indication of the expected spread in the $\sin^2\theta_W$ results from our real data samples. Using 200 pairs of data samples, we find the distribution of differences has a mean of 0.000 as expected and a sigma of 0.010. The difference between the results of our two data samples is thus a 1.6 sigma effect.

One may now ask whether there is a systematic difference in the two data samples. To address this question, one of us (E.K.) applied the electron cuts listed in Table 1 to the

Z_CAND.PRO_5_1 data sample, and compared event by event with the production sample. In the mass region $75\text{GeV} < M_{ee} < 105\text{GeV}$, there were 15 events in the Z_CAND.PRO_5_1 sample which were not in the production sample. Of these, 10 were absent because production did not process the raw data tape containing the event, and the remaining 5 did not pass the Electron_12 trigger.

We believe, then, that there are no large systematic differences between the production and Z_CAND.PRO_5_1 data samples. The difference in the production and Z_CAND.PRO_5_1 results are statistical differences, and the two results are consistent to within 1.6 sigma.

8 Radiative Corrections

There are many higher order diagrams which contribute to inclusive dielectron production in $\bar{p}p$ collisions. The QCD diagrams shown in Figure 6 produce dielectrons with non-zero transverse (to the beam direction) momentum, P_T. The order α^3 electroweak contributions to $q\bar{q} \rightarrow e^+e^-(\gamma)$ shown in Figure 7 are also a source of dielectron events. These higher order processes have a significant effect on the angular distribution of the dielectrons and the determination of $\sin^2\theta_W$. Initial state QCD radiation smears the $\cos\hat{\theta}$ values reconstructed from the electron 4-vectors, while the forward–backward asymmetry in $e^+e^- \rightarrow \mu^+\mu^-$ interactions at LEP can be approximately doubled by higher order QED processes [4], Furthermore, when higher order weak corrections are included, the values of $\sin^2\theta_W$ determined from different physical processes require/acquire different corrections, and care must be taken in comparing different measurements of $\sin^2\theta_W$.

The higher order corrections divide themselves naturally into QCD, QED, and weak corrections. The QCD corrections are independent of the electroweak corrections and can be treated separately. The electroweak corrections are more complex, and must be treated within the framework of a renormalization scheme. The on–shell renormalization scheme proposed by Marciano and Sirlin [17] and described in Reference [18] uses the fermion masses, α, M_Z, M_W, and M_{Higgs} as input parameters, and has the property that the QED diagrams are separable as a class. In this renormalization scheme, the QED sector is separately renormalizable, and QED quantities can be calculated independently of the remaining weak corrections. In the on–shell renormalization scheme, $\sin^2\theta_W$ is not an independent parameter, but is most naturally defined in terms of the W and Z^0 masses, by

$$\sin^2\theta_W \equiv 1 - \frac{M_W^2}{M_Z^2}. \tag{16}$$

In the subsequent sections, the effects of each of the different categories of higher order corrections on the forward–backward asymmetry and the interpretation of $\sin^2\theta_W$ are examined. The object of these correction procedures is first to account for higher order contributions to the measured asymmetry, and then to derive a value for a commonly accepted definition of $\sin^2\theta_W$ based on the corrected asymmetry.

8.1 QCD Corrections to the Asymmetry

The scattering angle $\hat{\theta}$ is defined to be the angle between the outgoing electron and incoming quark (or outgoing positron and incoming antiquark) in the rest frame of the electron pair. The initial quark directions, however, are not always well–defined in $p\bar{p}$ collisions. Due to the higher order QCD processes shown in Figure 6, Z^0's are produced with varying amounts of transverse momentum, P_T. When a Z^0 is produced with non–zero P_T, the proton and antiproton directions are not collinear in the rest frame of the dielectrons, and so the quark directions can not be completely determined; the quarks can only be said to be travelling in approximately the direction of the proton or antiproton, and the approximation gets worse as P_T increases. Since the initial quark directions are ill–defined, $\cos\hat{\theta}$ can no longer be precisely measured.

In practice, a new $\hat{z}$ axis is defined in the dielectron rest frame to take the place of the quark direction when making angular measurements. Several definitions for this axis have been proposed [5], among them the helicity frame in which $\hat{z}$ is taken along the recoil direction of the Z^0, and the Gottfried–Jackson frame in which $\hat{z}$ is taken along the proton direction. The definition used in this analysis is that of Collins and Soper [6], in which the $\hat{z}$ axis is taken to be the bisectrix of the proton and minus the antiproton directions. In effect, the Collins–Soper definition divides the P_T contribution equally between the quark and antiquark, and has the property that $\hat{z}$ reduces to the quark direction in the limit $P_T \rightarrow 0$.

All of these definitions of $\cos\hat{\theta}$ are approximations which begin to break down at high values of P_T. The $\cos\hat{\theta}$ distribution will be smeared somewhat by the high P_T events, and the measured asymmetry will be smaller than the true asymmetry due to this smearing. The size of this effect can be determined from the QCD corrected angular distribution.

There are several calculations of the differential cross section for Z^0 production and decay which include the diagrams of Figure 6, and incorporate the Collins–Soper definition of $\cos\hat{\theta}_{CS}$ explicitly [5, 6, 19]. Reference [19] gives the result [1] (for Z^0's only)

$$\begin{aligned}\frac{d\sigma}{d\cos\theta_{CS}\,dP_T} = {} & \frac{d\sigma}{dP_T}\Big\{[(((g_V^e)^2+(g_A^e)^2)((g_V^q)^2+(g_A^q)^2)] \\ & \times[(1+\cos^2\theta_{CS}+\tfrac{1}{2}A_0(1-3\cos^2\theta_{CS}))] \\ & +8g_V^e g_A^e g_V^q g_A^q(1-A_3)\cos\theta_{CS}\Big\}\end{aligned} \tag{17}$$

where $\frac{d\sigma}{dP_T}$ is the measured Z^0 P_T spectrum. A_0 and A_3 are functions of P_T and reduce to 0 as $P_T \rightarrow 0$. Plots of A_0 and A_3, taken from Reference [19], are shown in Figure 8. From this cross section a $\sin^2\theta_W$ independent, P_T dependent multiplicative correction factor for the asymmetry can be derived. Integrating Equation 6.2 over $\cos\hat{\theta}$ to find the measured

---

[1] The cross section also depends on ϕ, where ϕ is the azimuthal angle of the outgoing electron defined with respect to the plane containing the proton and antiproton in the rest frame of the electron pair. Equation 6.2 has been integrated over ϕ to remove this dependence.

asymmetry, one derives

$$A_{\mathrm{FB}}|_{Measured} = A_{\mathrm{FB}}|_{P_T=0} \int \frac{d\sigma}{dP_T} \left(1 - A_3\right) dP_T, \tag{18}$$

where $A_{\mathrm{FB}}|_{P_T=0}$ is the forward–backward asymmetry at $P_T = 0$.

The measured Z^0 P_T spectrum can be parametrized by a modified form of the P_T spectrum used in the ISAJET Monte Carlo. The data and the parametrization are shown in Figure 9[20]. Convolving the measured P_T spectrum with $(1 - A_3)$ as shown in Equation 6.3, the QCD corrections are found to reduce the measured asymmetry by a relative 1%. This implies that the measured value of $\sin^2\theta_W$ must be increased by 0.0003.

8.2 QED Corrections to the Asymmetry

The order α^3 QED contributions to $q\bar{q} \rightarrow e^+e^-(\gamma)$ are shown in groups III, IV, V, VI, and IX of Figure 7. They consist of all the graphs having an additional photon and the fermion loop correction to the photon propagator. To order α^3, the cross section has contributions from (1) the lowest order diagrams (which are of order α^2), (2) the interference between the lowest order diagrams and the diagrams having a photon or fermion loop (virtual diagrams), and (3) the diagrams having a real photon emitted from the initial or final fermions (Bremsstrahlung diagrams). The Bremsstrahlung diagrams have a 3–body final state, in contrast to the two–body final state of lowest order and virtual diagrams. The total cross section for $q\bar{q} \rightarrow e^+e^-(\gamma)$, then, is given by the sum of the two–body and three–body cross sections. Both the 2–body and 3–body cross sections are infrared divergent. These divergences cancel when the two cross sections are added, and so the total cross section is infrared–finite.

The bremsstrahlung contribution can be divided into a "soft" part and a "hard" part by a cutoff κ^0 in the energy of the emitted photon. The soft photons are not resolved by the detector, and appear as part of the electron shower in the calorimeter. This soft bremsstrahlung contribution is indistinguishable from a 2–body final state, and so it can be calculated analytically and added to the virtual cross section. The sum of the virtual and soft Bremsstrahlung contributions is infrared finite, as is the remaining hard Bremsstrahlung cross section.

The hard Bremsstrahlung photons are potentially very energetic, and can be produced at large angles to their parent fermions. The hard photons, then, can interact independently with the detector. Furthermore, the higher order soft contributions change the dielectron angular distribution in a non–trivial way, and thus the QED corrections to the asymmetry will depend on the detector geometry and acceptance. Because of these inherent detector dependences, the QED corrections are best studied with a Monte Carlo event generator which includes both hard and soft corrections, and a detector simulation.

8.2.1 Soft QED Corrections

The soft portion of the order α^3 QED cross section has been calculated by many authors for $e^+e^- \rightarrow f\bar{f}(\gamma)$ at LEP and SLC, but has been largely ignored for $q\bar{q} \rightarrow f\bar{f}(\gamma)$. This being the case, the LEP/SLC results are time–reversed to get predictions for $q\bar{q} \rightarrow e^+e^-(\gamma)$. The matrix elements for the virtual diagrams are invariant under time reversal, and so the published results can be used without change. The soft Bremsstrahlung contributions differentiate between initial and final state radiation, and require a little more care.

The soft corrections used in the current analysis have been taken from Reference [2]. The authors include all the diagrams in groups III, IV, V, VI and IX of Figure 7, and include the contribution of soft photons to all orders in α by exponentiation of the leading logarithms of the soft Bremsstrahlung terms as described in Reference [21].

In the LEP calculations, the soft initial state Bremsstrahlung corrections incorporate terms of the form

$$\frac{1}{M^2 - (s - 4E\kappa)} \tag{19}$$

where $M^2 = M_Z^2 - iM_Z\Gamma_Z$, E is the energy of the electron beams in the LEP accelerator, and s is the square of the center of mass energy of the machine. The term $(s - 4E\kappa)$ is interpreted as the effective Q^2 of the interaction after initial state Bremsstrahlung. Terms of this form enter the cross section in multiplicative scale factors and in a correction to the phase of the Z^0 resonance. The "prescription" for converting these terms to a form usable for $q\bar{q} \rightarrow e^+e^-$ interactions is to interpret E as the energy of the outgoing electrons in the center of mass frame, and s as the square of the dielectron invariant mass. The effective Q^2 of the interaction before final state Bremsstrahlung is then $(s + 4E\kappa)$. To convert the LEP calculations to $p\bar{p}$ calculations, one must change the sign of the κ term in the Bremsstrahlung coefficients, and to change the interpretation of s.

The forward–backward asymmetry is corrected in different ways by each of the types of QED diagrams. The virtual vertex corrections and the fermion loop corrections to the photon propagator can be absorbed into a renormalization of the photon coupling to fermions. This is an s dependent correction which affects both the symmetric and antisymmetric parts of the cross section and leaves the asymmetry unchanged.

The soft initial state Bremsstrahlung correction is an s dependent, multiplicative correction to the cross section which has no effect on the asymmetry. The soft final state Bremsstrahlung contribution has a multiplicative part which does not change the asymmetry, but it also affects the phase angle of the Z^0 resonance, which can affect the asymmetry. In the presence of soft final state brem, the Z^0 line shape grows a "shoulder" on the low mass side of the resonance, as shown in Figure 10. The shoulder is due to events produced on resonance which then radiate a photon as they decay; the reconstructed dielectron invariant mass of these events is decreased by the photon radiation. The asymmetry of the events in the shoulder region is characteristic of resonance production, and is larger than expected. This can be seen in Figure 11, where the the forward–backward asymmetry is plotted as a function of M_{ee}. The size of this effect increases as κ^0 increases.

The initial and final state Bremsstrahlung diagrams have different charge conjugation parities [22], and so the interference between these diagrams will contribute to the charge asymmetry. The size of the correction to the asymmetry from the radiative Z^0 diagrams is found to vary strongly with the cutoff κ^0 [23]; it is small for large values of κ^0 ($\delta A_{\mathrm{FB}} \simeq$

$0.00x\mathrm{at}\kappa^0 = 0.1$) but blows up when κ^0 is very small ($\kappa^0 < 10^{-3}$).

The QED box diagrams have an additional virtual photon propagator, and therefore have different charge conjugation parities from the lowest order diagrams with which they interfere. The box diagrams, then, also contribute to the observed charge asymmetry. The contribution is small ($\delta A_{\mathrm{FB}} \simeq 0.00x$) and is independent of $\sin^2\theta_W$ and κ^0.

It is convenient to show the QED corrections as a function of the charge asymmetry, A_C, where the charge asymmetry is defined by

$$A_C \equiv \frac{\left.\dfrac{d\sigma}{d\cos\hat{\theta}}\right|_{+\cos\hat{\theta}} - \left.\dfrac{d\sigma}{d\cos\hat{\theta}}\right|_{-\cos\hat{\theta}}}{\left.\dfrac{d\sigma}{d\cos\hat{\theta}}\right|_{+\cos\hat{\theta}} + \left.\dfrac{d\sigma}{d\cos\hat{\theta}}\right|_{-\cos\hat{\theta}}}. \tag{20}$$

This can be understood as a differential form of the forward–backward asymmetry A_{FB}; integrating over $\cos\hat{\theta}$, one finds

$$A_{\mathrm{FB}} = \int_0^1 A_C \, d\cos\hat{\theta}. \tag{21}$$

The corrected and uncorrected charge asymmetries on resonance for $\mathrm{u\bar{u}} \rightarrow e^+e^-$, $\mathrm{d\bar{d}} \rightarrow e^+e^-$, and $\mu\bar{\mu} \rightarrow e^+e^-$ are shown in Figure 12. The dashed lines show tree level calculations, while the solid lines include all the soft QED corrections evaluated at $\kappa^0 = 0.01$. The size of the QED corrections depends on the sign and magnitude of the initial fermion's charge. The corrections depend on $\cos\hat{\theta}$ in a complicated way, and so the total QED correction will depend on the acceptance of the detector and the analysis cuts.

8.2.2 Hard Corrections and the Radiative Monte Carlo

Hard photon emission smears the measured dielectron quantities; initial state Bremsstrahlung can disturb the reconstruction of $\cos\hat{\theta}$ by adding a small amount of transverse momentum, and final state Bremsstrahlung can directly affect the energy and direction of outgoing electrons. Unlike the soft corrections, which can either increase or decrease the asymmetry depending on the charges of the fermions in the interaction, the hard corrections always decrease the measured asymmetry by smearing the $\cos\hat{\theta}$ distribution. Since hard photons emitted in the process $f\bar{f} \rightarrow e^+e^-\gamma$ can interact in the detector and affect the measurement of electron quantities and $\hat{\theta}$, a proper treatment of the hard photon contribution requires a Monte Carlo event generator and a detector simulation.

The Monte Carlo generator used in this analysis is a modified version of the generator developed for the CDF Z^0 mass analysis [24]. It is based on the hard Bremsstrahlung calculations of [25] and includes the soft corrections of [2]. The hard Bremsstrahlung calculation includes only final state radiation. Hard initial state radiation has little effect on Z^0 production, and collinear photons from initial state radiation generally escape undetected down the beampipe. Large angle radiation from the quarks can produce transverse momentum P_T, which can affect the reconstruction of the final state in the manner described above for the QCD corrections. This effect is very small for photons, and is ignored in this analysis.

The Monte Carlo generates the proper 2 and 3 body angular distributions using a rejection method, and then weights each event by the convolution of the cross section with parton distribution functions. Since the angular part of the cross section is generated separately, the weight needs only account for the Q^2 dependence of the cross section. For the 2–body state, the cross section used in the weight is the soft QED cross section evaluated at $\cos\hat{\theta} = 0$. For the 3–body state, the cross section used is the lowest order cross section evaluated at $\cos\hat{\theta} = 0$ multiplied by $\delta^h_Q(\kappa^0)$, where $\delta^h_Q(\kappa^0)$ is the probability of producing a photon with energy fraction greater than κ^0, and is derived by integrating the photon spectrum from κ^0 to 1. Forms for the photon spectrum and $\delta^h_Q(\kappa^0)$ are given in Reference [25].

The Monte Carlo event generation proceeds as follows:

1. Values for x_1 and x_2, the fractional momenta of the quarks, are generated, and the resulting invariant mass is checked against the desired mass limits.

2. The event is assigned, with equal probability, to one of 4 possible production processes: (a) u quark from the proton, $\bar{u}$ quark from the antiproton, (b) d quark from the proton, $\bar{d}$ quark from the antiproton, (c) $\bar{u}$ quark from the proton, u quark from the antiproton, and (d) $\bar{d}$ quark from the proton, d quark from the antiproton. A weight is then calculated based on the parton distribution functions for u or d quarks and the fractional momenta calculated previously.

3. The event is chosen, with equal probability, to have a 2–body or 3–body final state.

4. The angular distribution of the outgoing particles is generated with a rejection procedure . For 2–body final states, the angular distribution of Reference [2] is used, while 3–body final states are generated according to the distribution of Reference [25].

5. A weight for the event is calculated from the cross section as a function of Q^2, as described above.

6. The overall weight for the event is calculated from the product of the the weight from the parton density functions and the weight from the cross section.

The final state 4–vectors and the event weight are the input for the detector simulation. The detector simulation must include the geometric features of the detector and the resolutions of the various detector elements, and must also be able to simulate the effects of the Bremsstrahlung photons. Moreover, it must be fast; the QED corrections require several million events to be simulated in order to achieve the desired statistical accuracy.

The detector simulation used in this analysis is a modified form of the simulation used to determine the acceptance. 2–body final states are simulated the same manner as the events used in the acceptance calculations. For the 3–body final states, the photon showers in the calorimeter and the effect of the photon on the electron measurement becomes important. For photons emitted at very small angles to the electron, the electron and photon showers are indistinguishable. The "electron" will be accepted by the analysis cuts, and the total energy measured by the calorimeter is the sum of the electron and photon energies. For photons with small energies, the effect of the photon on the electron measurement is small. The electron will pass the analysis cuts, and the photon will have little effect on the electron's energy or direction. For photons having an intermediate energy emitted at a moderate angle with respect to the electron, the effect of the photon is less clear. Electrons with energetic photons very near by may fail a shower shape cut like the strip χ^2 in the CEM or the 3×3 χ^2 in the PEM. Events with separated electron and photon showers may fail the isolation cut.

To study these effects, 20000 events were generated and fully simulated with the CDFSIM simulation package. The simulated events were then passed through the electron selection cuts used in this analysis. Using these simulated events, the photon angles and energies which still allow the electrons to pass the selection cuts can be identified. The available photon phase space can be parametrized, and the parametrization used quickly to accept or reject events. Figure 13 shows a plot of the photon–electron angle versus the fractional energy of the photon for electrons in the PEM which pass all of the selection cuts. Photons emitted at angles larger than 0.4 radians are outside the $R = 0.4$ isolation cone and have no effect on the electron measurement. Photons emitted at angles less than 0.4 radians, but having energies less than 10% of the electron's energy will also pass the isolation cut. Photons having energies larger than 10% of the electron energy must be emitted closely enough to the electron that the clustering routine will see only one electromagnetic cluster. Furthermore, the photon's energy must be low enough or its angle small enough that it pass the shower shape cuts. In general, as the photon's energy increases, the angle must decrease in order for the electron to pass the electron quality cuts. In the central region, the electron must also pass an E/P cut of 1.5. The photon energy, then, can never be greater than half of the electron's energy. The forbidden regions for photon emission in energy–angle space are shown in Figure 13.

The fast simulation of 3–body decays proceeds in the same fashion as the 2–body simulation, but with two extra steps: (1) if the photon is in the forbidden region of energy–angle space, the event is cut, and (2) if the photon is within ± 1 calorimeter η segment and within ± 1 calorimeter ϕ segment in the gas calorimeters, the photon and electron 4–vectors are summed to arrive at the measured "electron" 4–vector.

8.2.3 QED Results

The radiative Monte Carlo was used to calculate the forward–backward asymmetry for various values of $\sin^2\theta_W$, assuming $\kappa^0 = 0.01$. The results of these calculations is shown in Figure 14. The solid line shows the lowest order prediction for the asymmetry, assuming EHLQ 1 structue functions. The effect of the higher order QED diagrams is to reduce the observed asymmetry by a small amount, independent of $\sin^2\theta_W$. A fit to the Monte Carlo data yields the result

$$A_{\mathrm{FB}}|_{QED} = A_{\mathrm{FB}}|_{Born} - 0.0055 \,. \qquad (22)$$

The fit is indicated by the dashed curve in Figure 14. After removing the QED contribution to the asymmetry from the measured asymmetry, one arrives at the QED corrected results $A_{\mathrm{FB}} = 0.053$ and $\sin^2\theta_W = 0.231$.

The size of the QED corrections depends on the value of κ^0, as discussed above. The value chosen for κ^0, 0.01, is representative of the resolution of the detector and of various threshold cuts in the data collection and analysis procedures, but there is considerable latitude in the choice of κ^0. The systematic error on the QED contribution to the asymmetry associated with κ^0 was estimated using the radiative Monte Carlo. The forward–backward asymmetry was calculated at $\sin^2\theta_W = 0.230$ using various values of κ^0. Figure 15 shows the calculated asymmetry versus κ^0. The systematic error is chosen to be half the total spread in A_{FB}. This yields systematic errors of 0.0054 for A_{FB} and 0.0014 for $\sin^2\theta_W$.

8.3 Weak Corrections

The order α^3 weak corrections to $q\bar{q} \to e^+e^-$ are shown in groups VII, VIII, XI and XIII of Figure 7. These include the box and vertex diagrams having additional weak bosons as well as the fermion loop corrections to the weak boson propagators. As with the QED corrections, the vertex and propagator corrections can be absorbed into a renormalization of the Z^0 coupling to fermions and leave the asymmetry unchanged, while the box diagrams contribute to the measured asymmetry. Unlike the QED corrections, though, the renormalization of the Z^0 couplings is of more interest than the (small) changes in the asymmetry from the additional box diagrams. A renormalization of the Z^0 couplings to fermions implies a renormalization of $\sin^2\theta_W$, in which case both the value of $\sin^2\theta_W$ and its precise definition may change.

In order to perform a meaningful calculation of the weak corrections, one must choose both a definition for $\sin^2\theta_W$ and a renormalization scheme. For the asymmetry analysis, the on–shell renormalization scheme proposed by Marciano and Sirlin [17] and documented in Reference [18] is used. In this renormalization scheme $\sin^2\theta_W$ not an independent parameter, but is defined, to all orders in perturbation theory, by

$$\sin^2\theta_W|_{MS} \equiv 1 - \frac{M_W^2}{M_Z^2}. \tag{23}$$

This is not the most convenient definition of $\sin^2\theta_W$ for an analysis of Z^0 data. The W mass has a rather strong (quadratic) dependence on the mass of the top quark, due to the t–b loop contribution to the W self energy shown in Figure 16, while the Z^0 mass (and other Z^0 observables) depend only weakly on the top mass. When determining $\sin^2\theta_W$ from one of the Z^0 observables, one must incorporate the m_t dependence of M_W into the calculation. As a result, *sinms* will also have a quadratic dependence on the top mass. Most of the existing measurements of $\sin^2\theta_W$ have been made using the Marciano–Sirlin definition $\sin^2\theta_W|_{MS}$, however, and so for purposes of comparison with these results the Marciano–Sirlin definition is used in the asymmetry analysis.

The order α^3 weak cross section is calculated in Reference [18] for $e^+e^- \to f\bar{f}$. As with the virtual QED diagrams, the matrix elements for the weak diagrams are invariant under time reversal, and so the results of [18] can be used directly to calculate the corrections to $q\bar{q} \rightarrow e^+e^-$. By integrating the corrected cross section numerically over structure functions, Q^2, and $\cos\hat{\theta}$ one can calculate the forward–backward asymmetry for given values of the fermion masses, the Higgs mass, and the masses of the W and Z^0.

To calculate the value of $\sin^2\theta_W|_{MS}$ as a function of the mass of the top quark, we solve iteratively for the value of $\sin^2\theta_W|_{MS}$ which generates the observed asymmetry. A plot of $\sin^2\theta_W|_{MS}$ versus top mass is shown in Figure 17. This result can be compared to the value of $\sin^2\theta_W|_{MS}$ determined directly from the W and Z masses, $\sin^2\theta_W|_{MS} = 0.230 \pm 0.008$[26]. The agreement is very good up to large top masses ($m_t \simeq 200$ GeV).

9 Asymmetries away from the Z^0

The γZ interference term in the cross section of Equation 4 has an antisymmetric term, which can lead to observable asymmetries away from the region of the Z^0 resonance. Indeed, these asymmetries have been reported by many e^+e^- experiments [27]. A distinguishing characteristic of the interference term is that it changes sign as one moves through the Z^0 pole. One thus expects that the asymmetry will also change sign as one moves through the Z.

We have divided our data sample into three mass regions, and have calculated the asymmetry in each. In the region $60 < M_{ee} < 75$ GeV, we find 5 events with $\cos\hat{\theta} > 0$ and 8 events with $\cos\hat{\theta} < 0$. Using the event counting method described in Section 5 and ignoring acceptance effects we find $A_{FB}|_{60-75} = -0.23 \pm 0.27$. In the region $M_{ee} > 105$ GeV, we find 10 events with $\cos\hat{\theta} > 0$ and 1 event with $\cos\hat{\theta} < 0$, yielding the value $A_{FB}|_{105\rightarrow} = 0.75 \pm 0.23$. Note that no background subtraction has been made in these two regions; Kearns *et. al.* estimates that there are of order 3 background events in the lower region. In the region of the Z^0 we have measured $A_{FB}|_{75-105} = 0.047 \pm 0.059$. We plot these values for the asymmetry versus the average mass in each mass region in Figure 18. The solid line is the theoretical prediction from Equation 4, assuming EHLQ1 structure functions. We see that the asymmetry does indeed change sign as one passes through the Z, and agrees well with the theoretical prediction.

While the agreement between experiment and theory is good away from the Z^0, it is difficult to extract any additional information from this region. The asymmetric term in the interference contribution to the cross section contains only the axial couplings of the fermions to the Z^0; the contribution of the vector couplings is symmetric and is small when compared to the photon contribution. Thus, no additional information on the value of $\sin^2\theta_W$ is contained in the asymmetries away from the Z^0. Furthermore, it is believed that a new neutral gauge boson will be best investigated through studies of the dilepton invariant mass distribution [28], rather than through its effects on the Z^0 asymmetry. The agreement in the asymmetry away from the Z^0 pole does, however, lend confidence to the measurement of the asymmetry at the Z^0 itself

10 Conclusions

We have measured the value $\sin^2\theta_W = 0.231 \pm 0.016\,(\mathrm{stat}) \pm 0.002\,(\mathrm{sys})$ from a fit to the angular distribution of electron pairs in Z^0 events, and have removed the contribution of higher order QED diagrams. The largest source of systematic error is the κ^0 dependence of the QED corrections. We can directly compare this value of $\sin^2\theta_W$ with other measurements derived from the Z^0 asymmetry. Using 33 selected $Z^0 \to e^+e^-$ and $Z^0 \to \mu^+\mu^-$ events, UA1 has measured $\sin^2\theta_W = 0.24^{+0.05}_{-0.04}$[29]. More recently, the L3 collaboration has combined measurements of the partial width of Z^0 decays into leptons, Γ_{ll}, and the forward–backward asymmetry in $Z^0 \to \mu^+\mu^-$ and $Z^0 \to \tau^+\tau^-$ decays to derive values for the couplings g_V^e and g_A^e. L3 finds $g_V^e = 0.00 \pm 0.07$, and $g_A^e = -.515 \pm 0.015$ [30]. Using the definitions for the coupling constants in terms of $\sin^2\theta_W$ given in Equation 3, the L3 measurement becomes $\sin^2\theta_W = 0.26 \pm 0.07$. After weak corrections, our value of $\sin^2\theta_W|_{MS}$ agrees well with that obtained from the measurement of the W and Z masses, up to large top masses ($m_t \simeq 200$ GeV).

We have investigated the possibility of using the asymmetry in $p\bar{p} \to e^+e^-$ to directly measure the Z^0 couplings to quarks. The asymmetry we measure depends on six different fermion couplings: the vector and axial vector couplings to both u–type and d–type quarks, and the couplings to electrons. We therefore would need five measurements or constraints in addition to the asymmetry measurement in order to derive values for all of the couplings. Using so much additional information to derive these values trivializes the process somewhat, and little new information is extracted from the asymmetry measurement. It is most appropriate simply to conclude that the asymmetry measurement, which depends strongly on the quark couplings, is in very good agreement with the Standard Model predictions and the world average value for $\sin^2\theta_W$.

References

[1] S.L. Glashow, Nucl. Phys. **B 22**, 579 (1961);
S. Weinberg, Phys. Rev. Lett. **19**, 1264 (1967);
A. Salam, in *Elementary Particle Theory*, edited by N. Svartholm (Almquist and Wiskell, Stockholm, 1968), p.367

[2] M. Böhm, W. Hollik, Nucl. Phys. **B 204**, 45 (1982)

[3] V. D. Barger and R. J. N. Phillips, *Collider Physics* (Addison–Wesley, Reading, Massachusetts, 1987)

[4] R. D. Peccei, DESY preprint DESY 89-043 (1989)

[5] M. Chaichian, M. Hayashi, and K. Yamagishi, Phys. Rev. **D 25**, 130 (1982)

[6] J.C. Collins and D.E. Soper, Phys. Rev. **D 16**, 2219 (1977)

[7] The energy corrections applied by ELENCR are documented in
T. Kamon, **CDF 905**, CEMMAP Description - CEM response map corrections
S. Kim *et. al.*, **CDF 906**, Electron energy correction with PEM response map ⋯
T. Kamon, S. Kim, **CDF 892**, Electron energy correction in PEM dead layers

[8] J. Proudfoot, F. Ukegawa, A. B. Wicklund, **CDF 933**, Central strip chamber alignment

[9] CDF note in preparation

[10] E. Kearns, M. Franklin, P. Hurst, J. Ng, **CDF 1097** $\sigma \cdot B(Z^0 \rightarrow e^+e^-)$

[11] F. Paige and S.D. Protopopescu, BNL Report No. BNL 38034, 1986 (unpublished)

[12] J. Proudfoot, **CDF 1008**, Central Electron 12 GeV Trigger Efficiency

[13] C. Blocker, **CDF 1115**, Measurement of the Z Asymmetry using e^+e^- Events

[14] E. Eichten, I. Hinchliffe, K. Lane, and C. Quigg, Rev. Mod. Phys. **56**, 579 (1984);
D.W. Duke and J.F. Owens, Phys. Rev. **D 30**, 49 (1984);
M. Diemoz, F. Ferroni, E. Longo, and G. Martinelli, Z. Phys. **C 39**, 21 (1988);
A. D. Martin, R. G. Roberts, and W. J. Stirling, Mod. Phys. Lett. **A 4**, 1135 (1989)

[15] See, for example,
P. Hurst, **CDF 1097**, Asymmetry in Z^0 decay at CDF

[16] R. J. Cashmore, C. M. Hawkes, B. W. Lynn, R. G. Stuart, Z. Phys. **C 30**, 125 (1986)

[17] W. J. Marciano, Phys. Rev. **D 20**, 274 (1979)
A. Sirlin, Phys. Rev. **D 22**, 971 (1980)
W. J. Marciano, A. Sirlin, Phys. Rev. **D 22**, 2695 (1980)

[18] W. F. L. Hollik, DESY Preprint DESY 88-188

[19] P. Chiappetta, M. Le Bellac, Z. Phys. **C 32**, 521 (1986)

[20] J. Ng, private communication

[21] M. Greco, G. Pancheri-Srivastava, Y. Srivastava, Nucl. Phys. **B 171**, 118 (1980)

[22] F. A. Berends, K. J. F. Gaemers, R. Gastmans, Nucl. Phys. **B 63**, 381 (1973)

[23] M. Böhm, W. Hollik, in *Z Physics at LEP 1*, CERN 89-08, Volume 1, p 203, (1989)

[24] R. G. Wagner, unpublished

[25] F. A. Berends, R. Kleiss, Z. Phys. **C 27**, 365 (1985);
F. A. Berends *et. al.* Z. Phys. **C 27**, 155 (1985)

[26] F. Abe *et. al.*, in preparation

[27] See, for example,
M.E. Levi et al., Phys. Rev. Lett. **51**, 1941 (1983)
W. Bartel et al., Phys. Lett. **108B**, 140 (1982)
B. Adeva et al., Phys. Rev. Lett. **48**, 1701 (1982)
H.J. Behrend et al., Phys. Lett. **114B**, 282 (1982)

[28] J. Rosner, Phys. Lett. **221B**, 85 (1989)

[29] T. Müller, Fortschr. Phys. **37**, 339 (1989)

[30] L3 Collaboration, L3 Preprint # 003

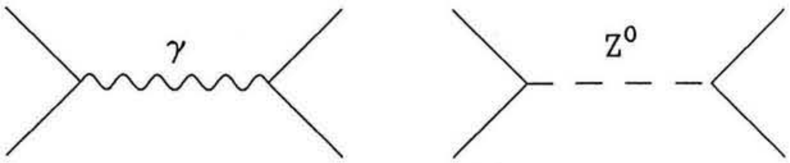

Figure 1: Lowest order Feynman diagrams for $p\bar{p} \rightarrow e^+e^-$

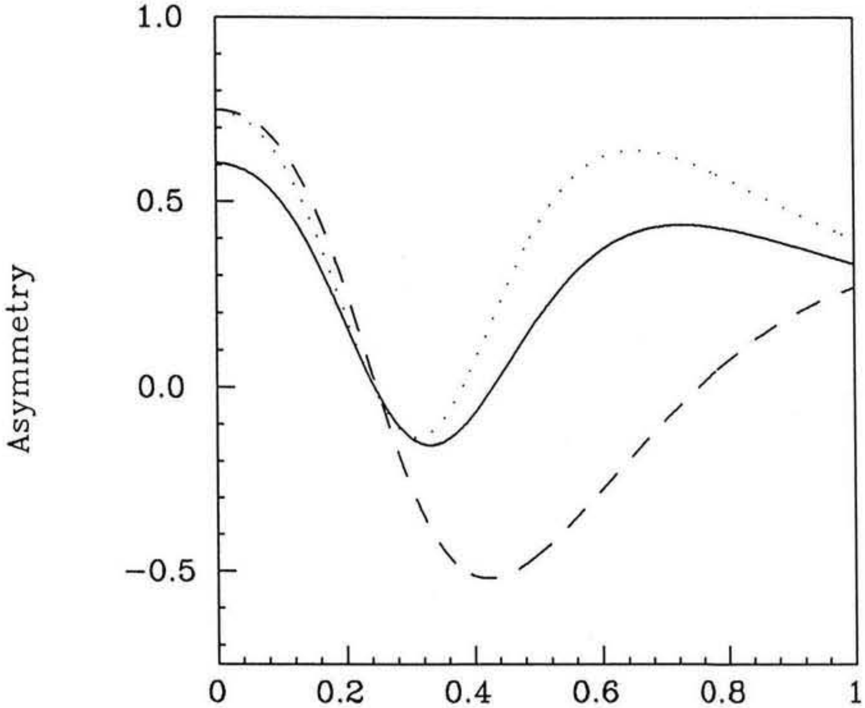

Figure 2: Asymmetry as a function of $\sin^2\theta_W$. The dotted curve shows the u–type asymmetry while the dashed curve shows the asymmetry for d–type quarks. The solid curve is the observed asymmetry for EHLQ 1 structure functions.

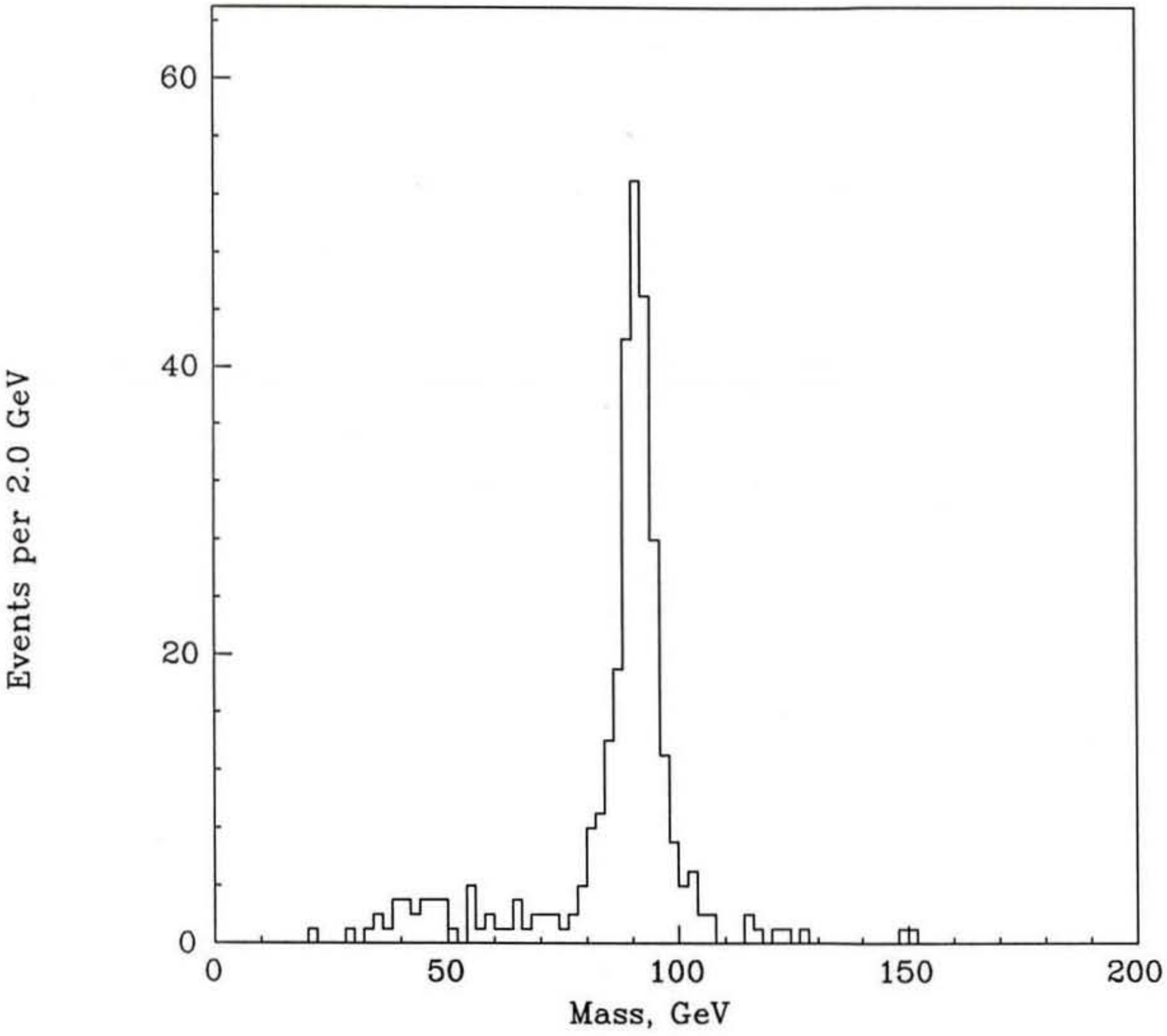

Figure 3: Dielectron invariant mass

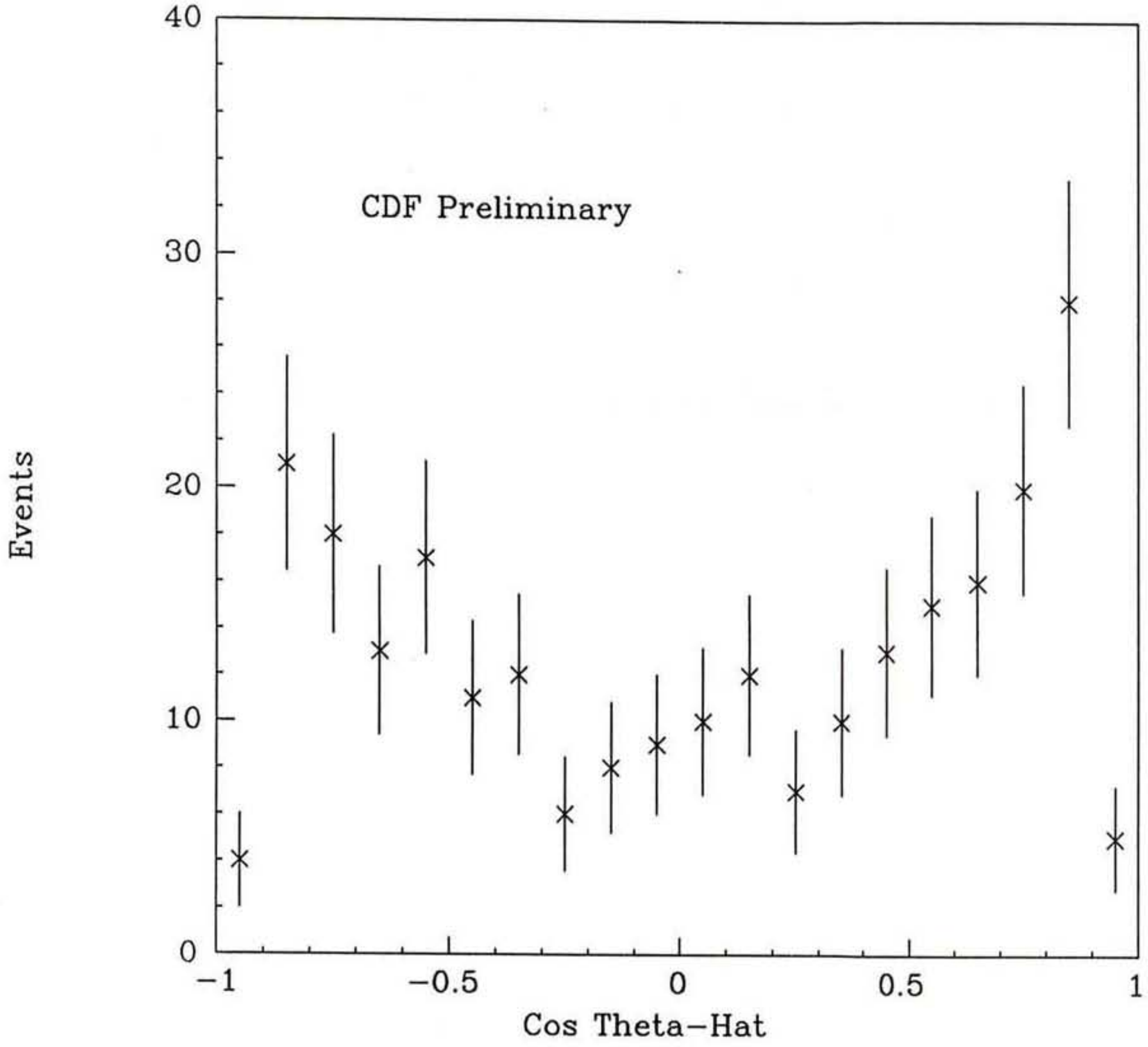

Figure 4: Uncorrected $\cos\hat{\theta}$ distribution

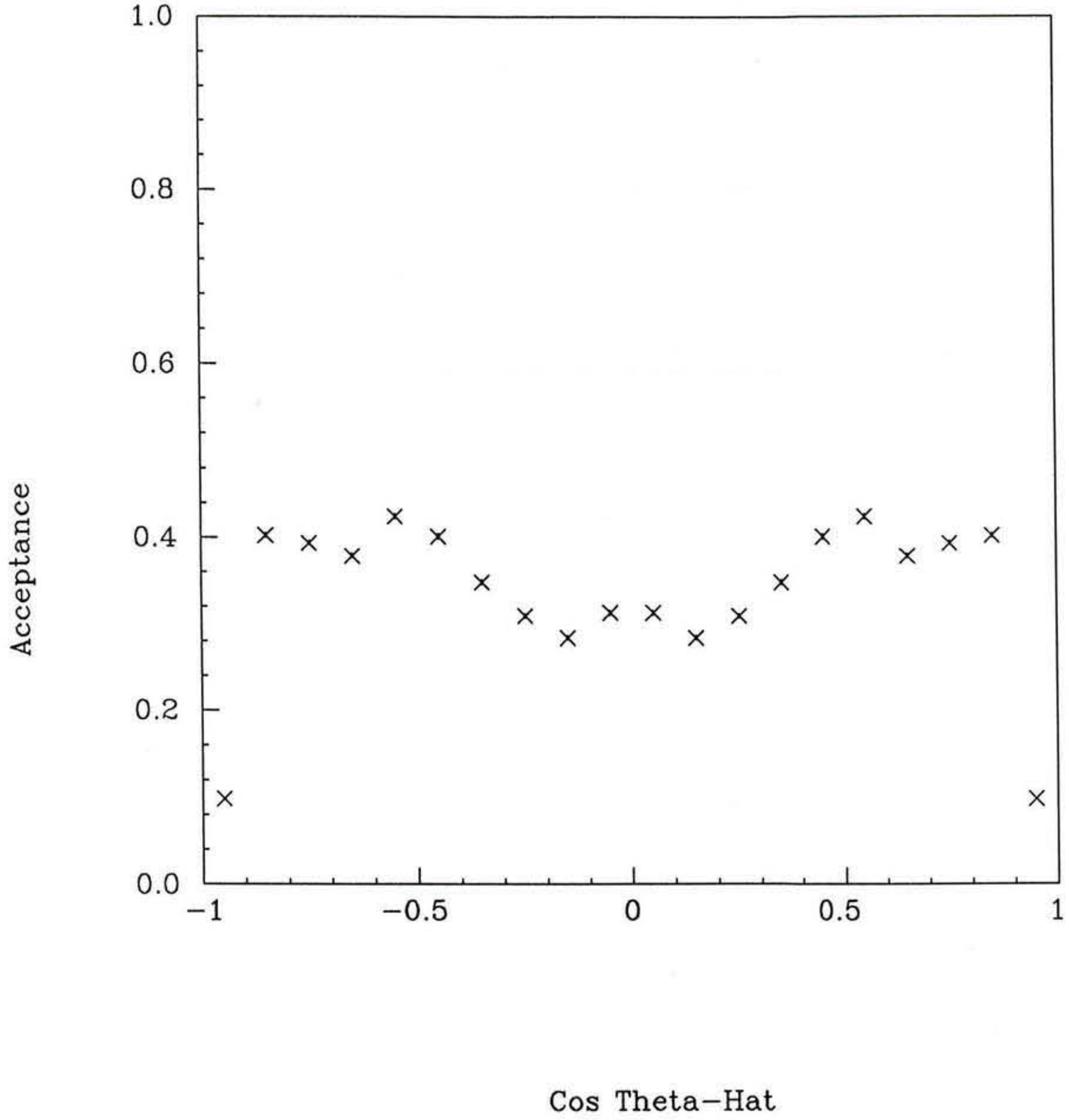

Figure 5: Acceptance as a function of $\cos\hat{\theta}$

Figure 6: Next order QCD diagrams

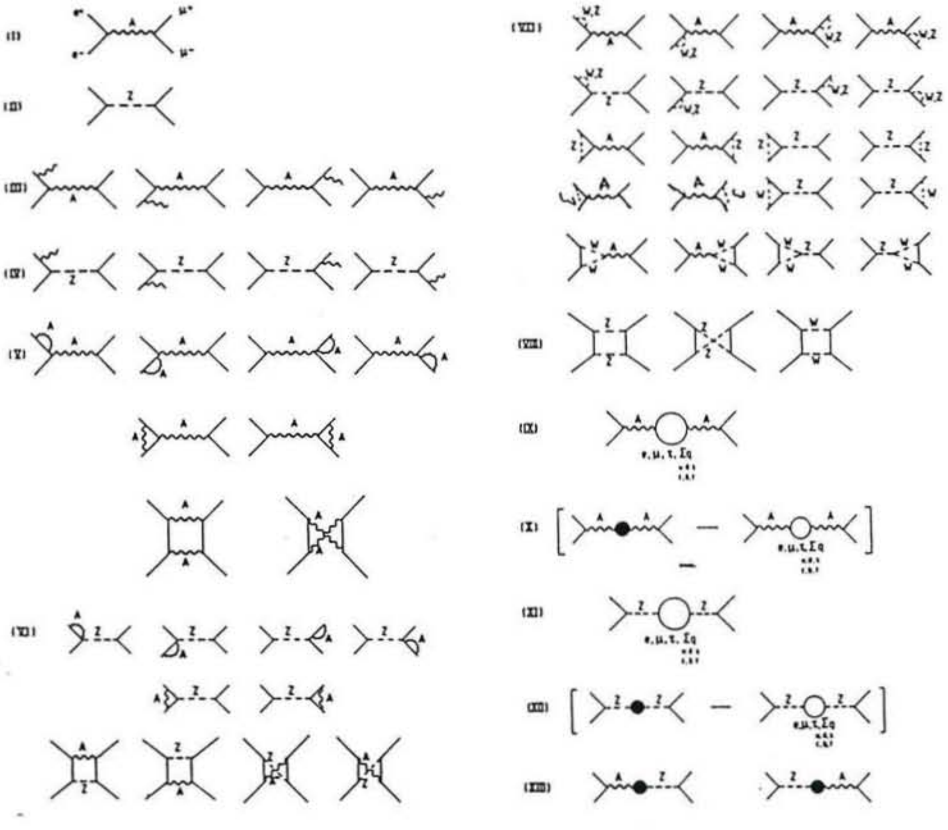

Figure 7: Diagrams contributing to $q\bar{q} \to e^+e^-$. Taken from Reference [16]

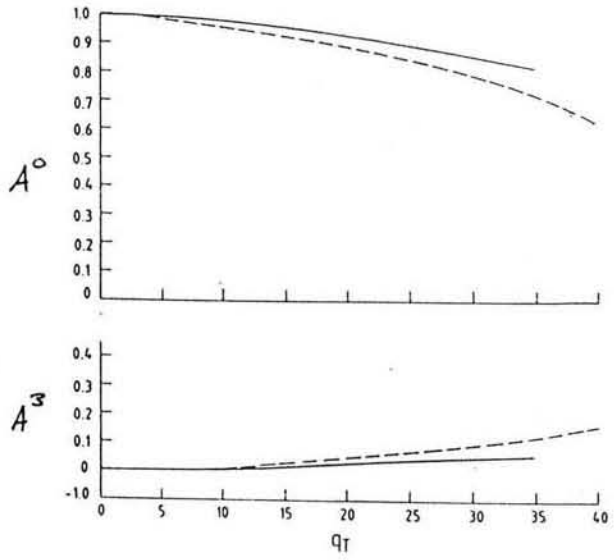

Figure 8: A^0 and A^3, for 630 GeV (solid) and 2 TeV (dash) taken from Reference [19].

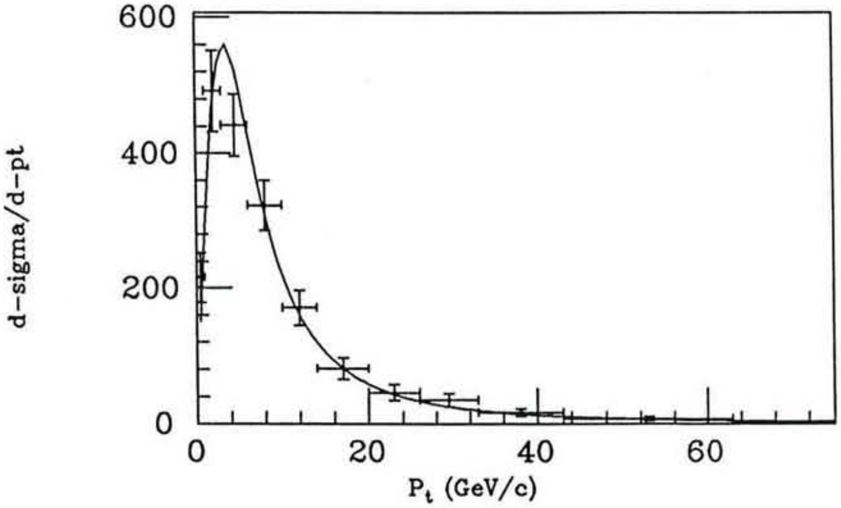

Figure 9: Measured Z^0 transverse momentum and fit

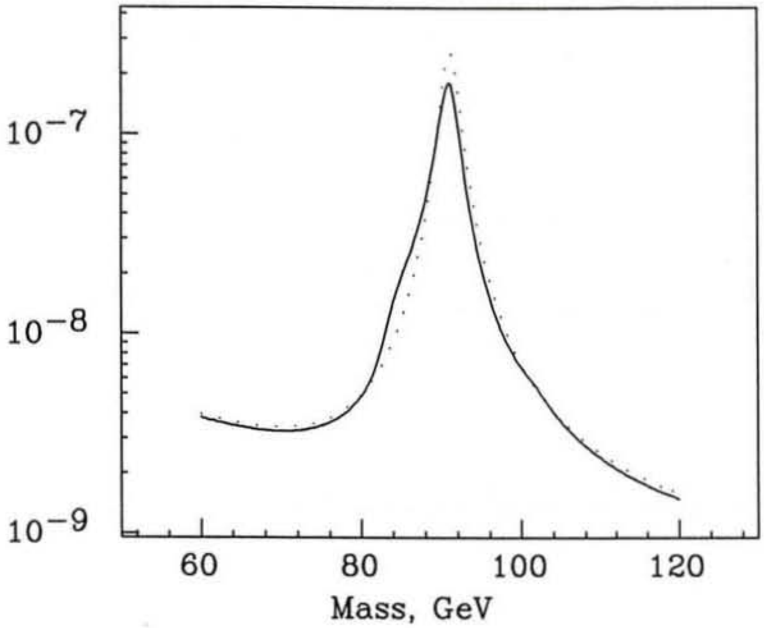

Figure 10: Invariant mass with and without soft QED corrections

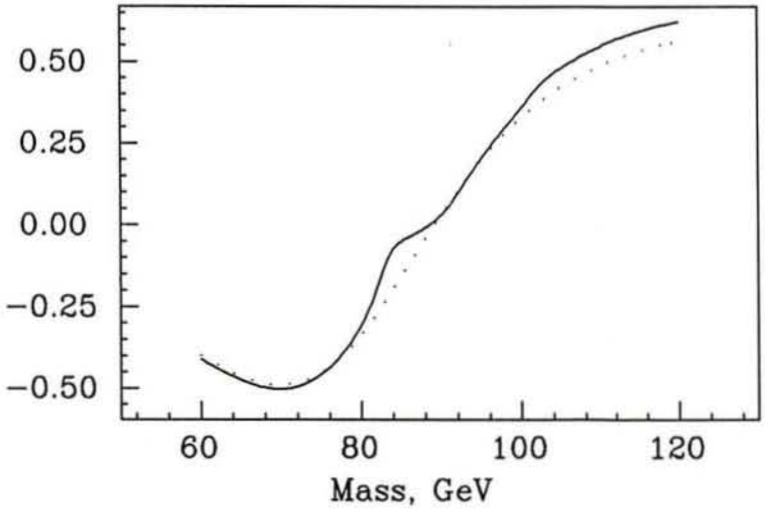

Figure 11: Asymmetry with and without soft QED corrections

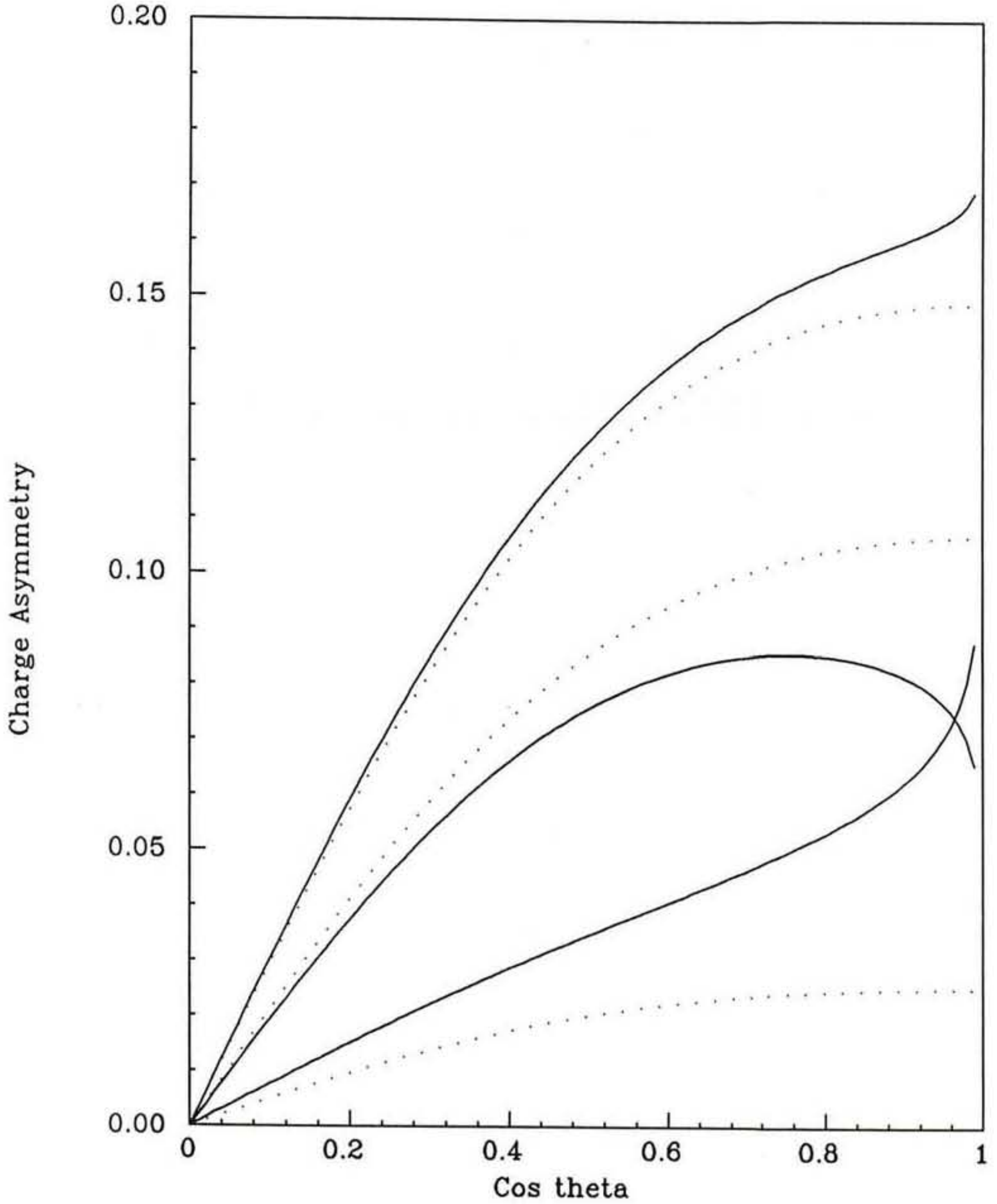

Figure 12: Charge asymmetries before (dashed) and after (solid) QED corrections

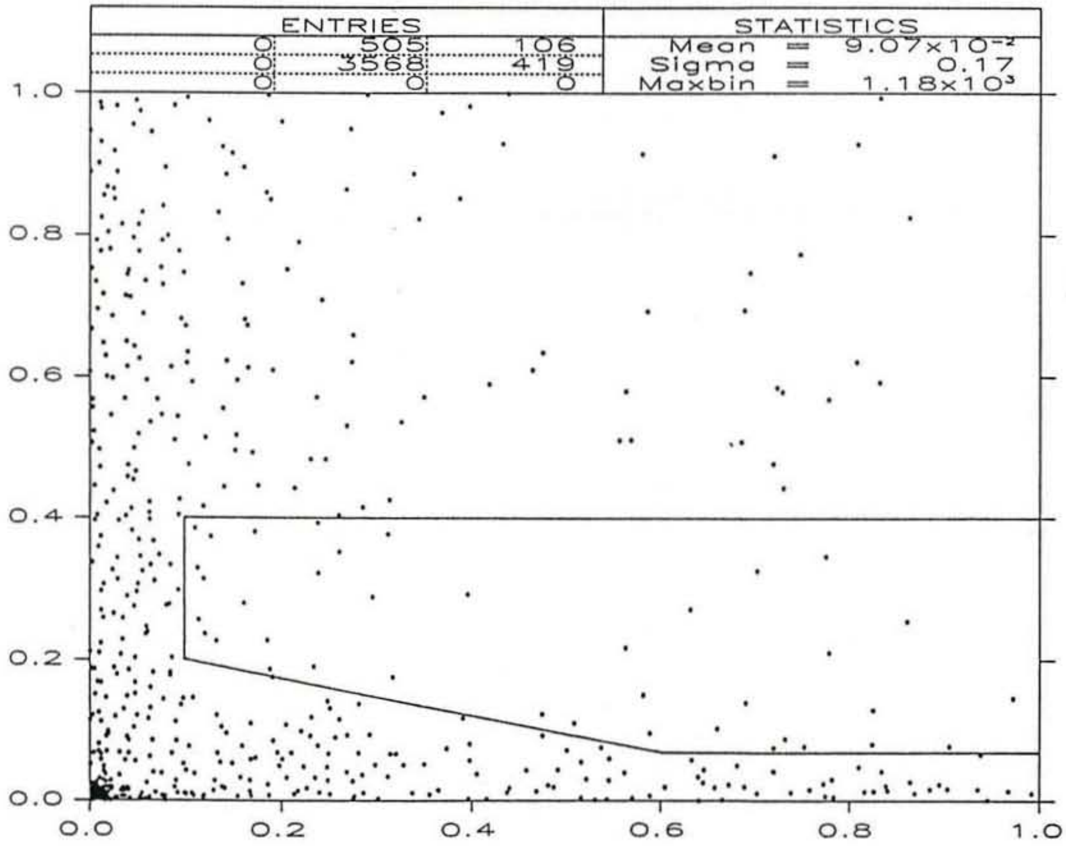

Figure 13: Photon angle versus fractional momentum of photon for electrons passing quality cuts

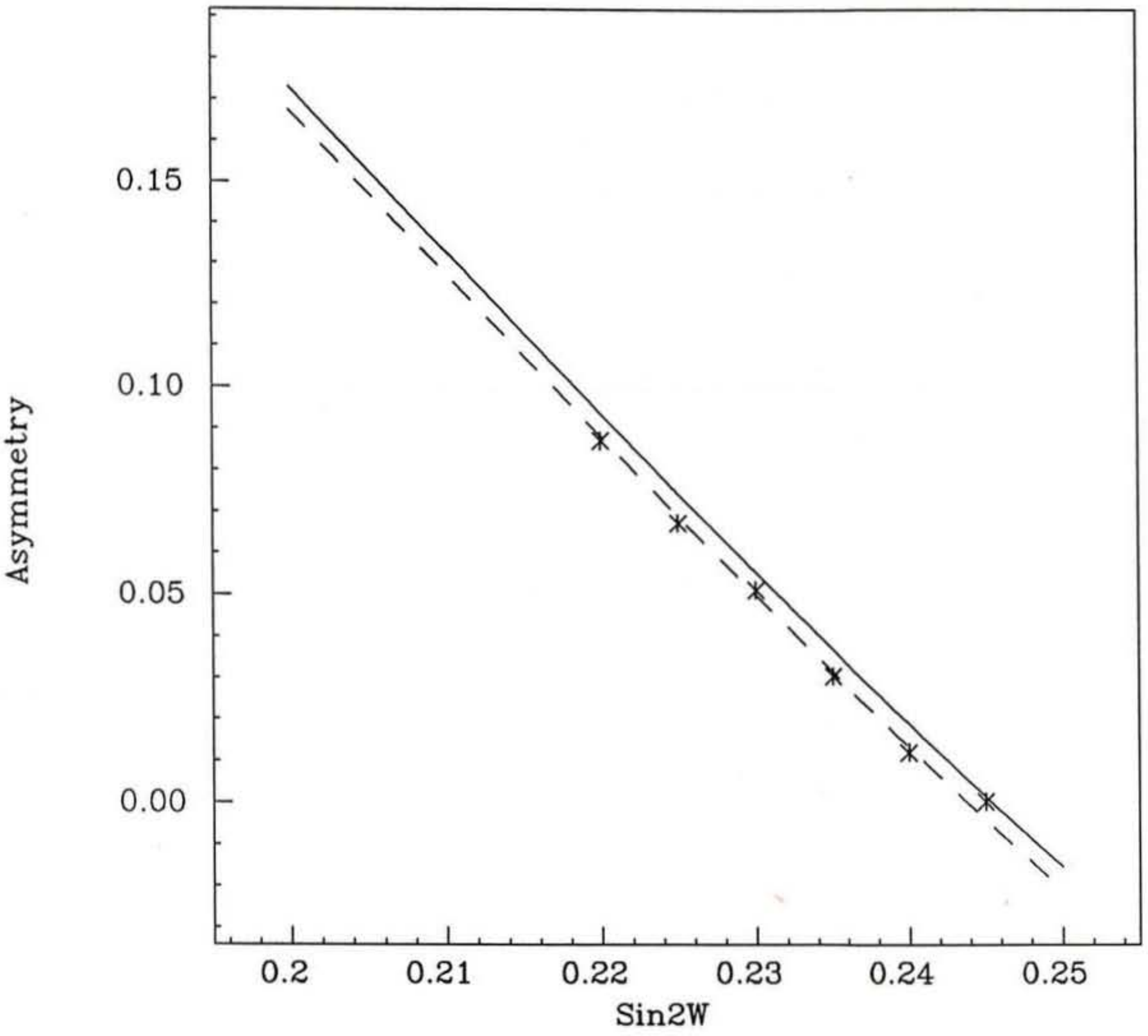

Figure 14: Asymmetry versus $\sin^2\theta_W$ with QED corrections

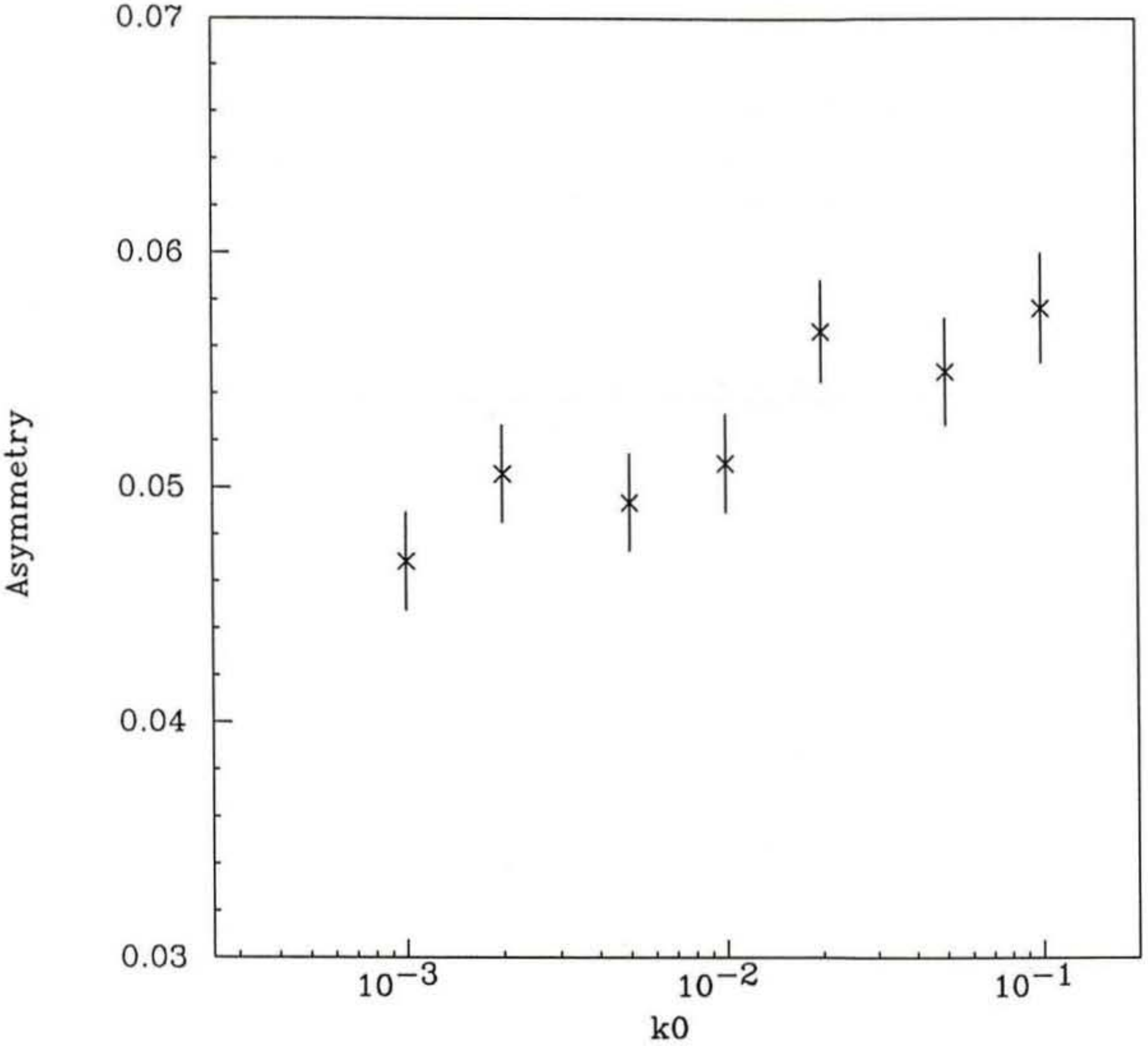

Figure 15: Asymmetry versus κ^0

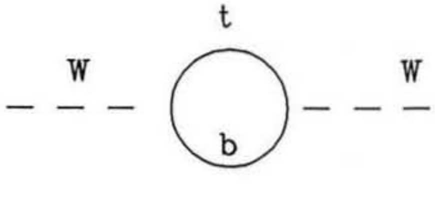

Figure 16: t–b loop in renormalized W propagator

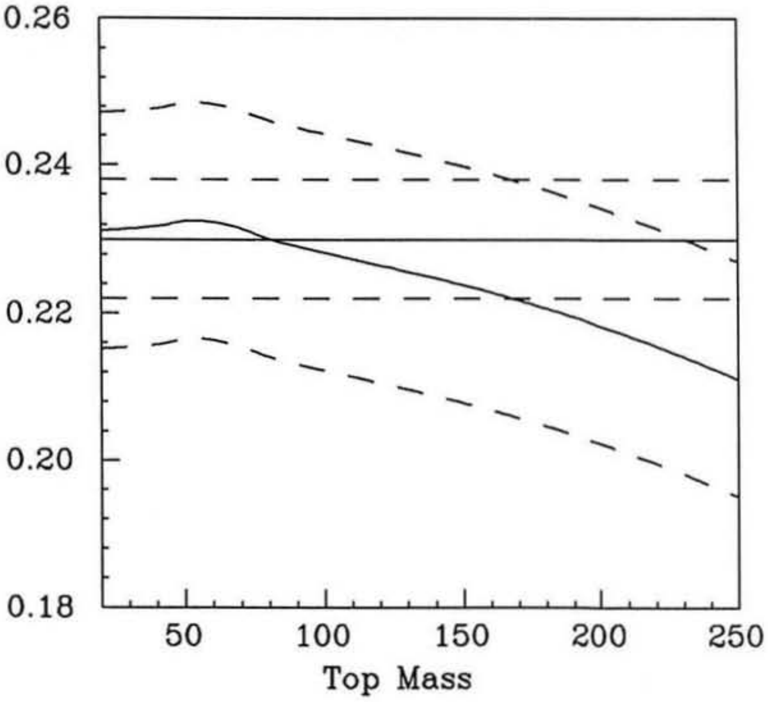

Figure 17: $\sin^2\theta_W|_{MS}$, derived from the forward–backward asymmetry

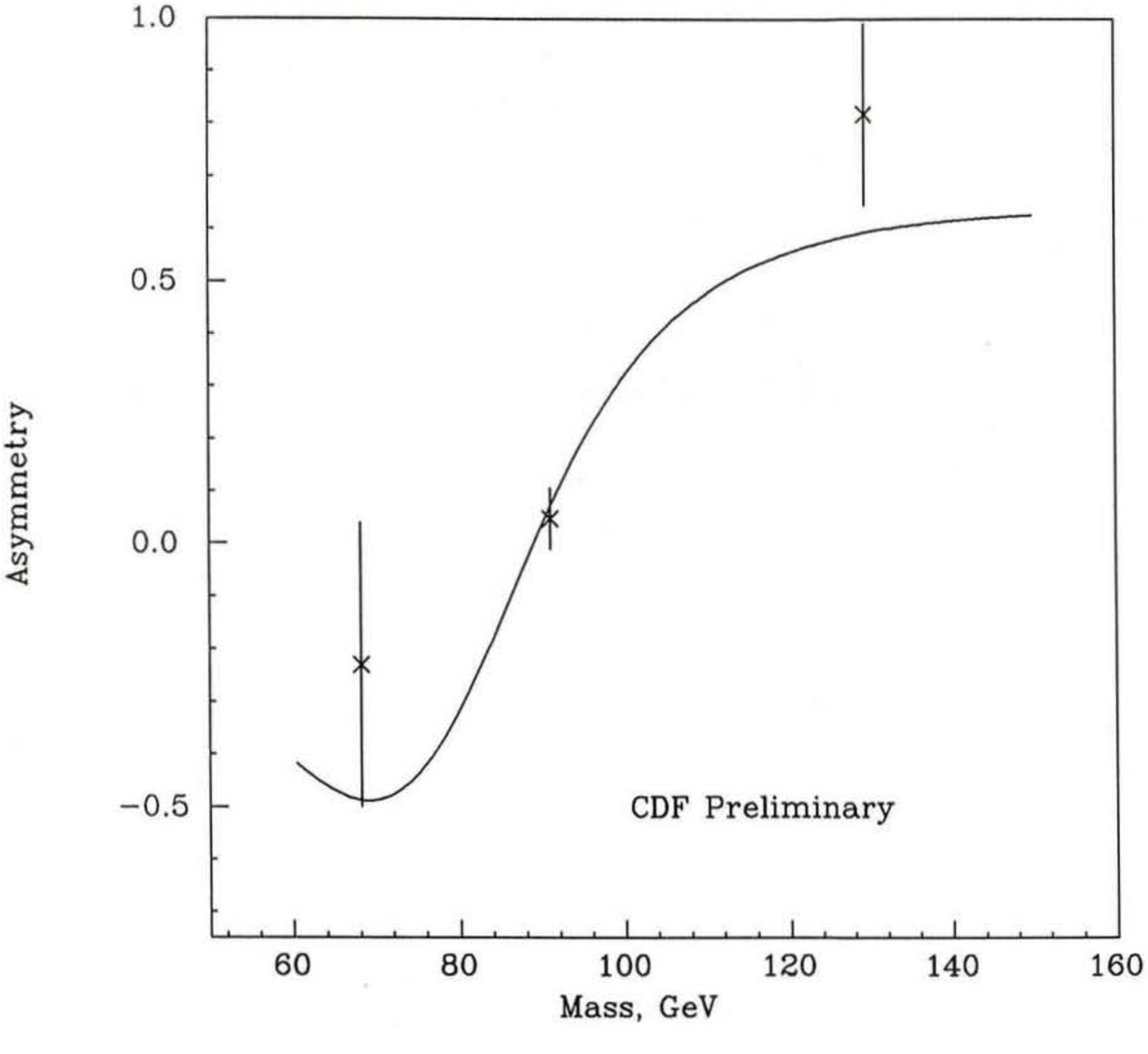

Figure 18: The forward–backward asymmetry as a function of invariant mass